nature communications

Article

https://doi.org/10.1038/s41467-025-57533-y

Aggregation induced emission luminogen bacteria hybrid bionic robot for multimodal phototheranostics and immunotherapy

Received: 18 July 2024

Accepted: 25 February 2025

Published online: 16 March 2025

Check for updates

Liwei Zhu[1,6], Guangjie Song[2,6], Wentian Zhang[1], Yifan Wu[1], Yuling Chen[1], Jiayi Song[1], Deliang Wang[3], Guoxin Li[4] ✉, Ben Zhong Tang[5] ✉ & Ying Li[1] ✉

Multimodal phototheranostics utilizing single molecules offer a "one-and-done" approach, presenting a convenient and effective strategy for cancer therapy. However, therapies based on conventional photosensitizers often suffer from limitations such as a single photosensitizing mechanism, restricted tumor penetration and retention, and the requirement for multiple irradiations, which significantly constrain their application. In this report, we present an aggregation-induced emission luminogen (AIEgen) bacteria hybrid bionic robot to address above issues. This bionic robot is composed of multifunctional AIEgen (INX-2) and *Escherichia coli* Nissle 1917 (EcN), i.e., EcN@INX-2. The EcN@INX-2 bionic robot exhibits near-infrared II (NIR-II) fluorescence emission and demonstrates efficient photodynamic and photothermal effects, as well as tumor-targeting capabilities. These features are facilitated by the complementary roles of INX-2 and EcN. The robot successfully enables in vivo multimodal imaging and therapy of colon cancer models in female mice through various mechanisms, including the activation of anti-tumor immunity, as well as photodynamic and photothermal therapy. Our study paves an avenue for designing multifunctional diagnostic agents for targeted colon cancer therapy through image-guided combinational immunotherapy.

Malignant neoplasms pose a serious threat to human health and are one of the leading causes of death worldwide[1]. Traditional modalities such as surgery, chemotherapy, and radiotherapy are frequently encumbered by challenges related to efficacy, side effects, and poor patient prognosis. This has intensified the need for more effective cancer therapies[2]. Phototherapy is a non-invasive approach minimally impacting healthy tissues, targeting exclusively the irradiated region, thereby aligning with the principles of precision medicine[3,4]. In recent years, photodynamic therapy (PDT) and photothermal therapy (PTT) have garnered considerable attention for their potential to overcome many of the limitations associated with traditional treatments[5,6]. The synergistic combination of PDT and PTT has shown promising potential, as the thermal effects of PTT augment oxygen supply, thereby boosting the effectiveness of PDT[7–9]. Such agents not only streamline the therapeutic process but also augment efficacy by inducing immunogenic cell death (ICD)[10] and stimulating immune

[1]Innovation Research Center for AIE Pharmaceutical Biology, Guangzhou Municipal and Guangdong Provincial Key Laboratory of Molecular Target & Clinical Pharmacology, the NMPA and State Key Laboratory of Respiratory Disease, School of Pharmaceutical Sciences and the Second Affiliated Hospital, Guangzhou Medical University, Guangzhou, Guangdong 511436, China. [2]Center for AIE Research, Shenzhen Key Laboratory of Polymer Science and Technology, Guangdong Research Center for Interfacial Engineering of Functional Materials, College of Materials Science and Engineering, Shenzhen University, Shenzhen 518060, China. [3]Department of Materials Chemistry, Huzhou University, Huzhou, Zhejiang 313000, China. [4]Cancer Center of Beijing Tsinghua Changgung Hospital, School of Clinical Medicine, Tsinghua Medicine, Tsinghua University, Beijing 102218, China. [5]School of Science and Engineering, Shenzhen Institute of Aggregate Science and Technology, The Chinese University of Hong Kong, Shenzhen (CUHK-Shenzhen), Guangdong 518172, China. [6]These authors contributed equally: Liwei Zhu, Guangjie Song. ✉e-mail: gzliguoxin@163.com; tangbenz@cuhk.edu.cn; liying@gzhmu.edu.cn

responses[11,12]. By promoting the maturation of dendritic cells (DCs) and the activation of T cells[13], ICD significantly enhances T cell-mediated antitumor immunity[14,15]. Photosensitizers (PSs) possess the potential to induce oxidative stress within cancer cells, thereby triggering ICD[16,17]. The potency of the immune response elicited by ICD is intricately tied to the generation of reactive oxygen species (ROS)[18,19]. However, the intricacy inherent in the combination of diverse components renders the synergistic therapeutic process convoluted and protracted, potentially heightening in vivo toxic side effects[20]. In this context, the urgent development of multifunctional single-component therapeutic agents capable of harmonizing PDT and PTT at a singular excitation wavelength is imperative[21,22].

Aggregation-induced emission (AIE) has become a groundbreaking concept in biophotonics, especially in cancer therapeutics[23,24]. AIE luminogens (AIEgens) exhibit distinctive features, including intramolecular motion units and complex, twisted three-dimensional structures that minimize intermolecular interactions and molecular mobility[25,26]. These agents, through careful design, are able to integrate dual roles of PDT and PTT[7,8]. Additionally, AIEgens offer multimodal imaging capabilities, including near-infrared (NIR) fluorescence imaging (FLI), photoacoustic imaging (PAI) and photothermal imaging (PTI)[7,8]. These imaging techniques provide complementary views into tumor biology and the microenvironment, and aid in accurate tumor detection and therapeutic response monitoring[27–29]. For example, FLI provides high spatial resolution and sensitivity[30], PAI excels in deep tissue penetration and contrast[31], and PTI monitors temperature changes during PTT[29], thereby enhancing the precision of cancer treatment[32,33]. In conclusion, AIEgens can enable efficient ICD with the synergistic effect of PDT and PTT under multimodal imaging guidance[34,35], making them essential tools for tumor treatments. Despite the robust properties of AIEgens like enhanced fluorescence and photostability, the acidic, hypoxic, and abnormal vascular tumor microenvironment impede drug delivery, leading to therapeutic resistance and immune suppression within tumors[25,26]. Moreover, systemically administered AIEgens lack tumor cell specificity and may pose toxic risks to healthy tissues[36]. Therefore, improving the tumor-targeting ability and efficacy of AIEgens is a significant challenge that remains to be addressed.

In recent years, biological carriers, including cells, bacteria, and viruses[37,38], have attracted considerable attention in tumor therapy due to their ability to naturally target and accumulate within tumor tissues[8,39–44]. Among these, bacteria-mediated cancer therapy stands out as a highly promising biotherapeutic strategy. Certain bacterial genera, such as *Escherichia, Salmonella, Listeria, Clostridium*, and *Bifidobacterium*, show a natural propensity for tumor targeting, selectively accumulating within tumor tissues[45–48]. *Escherichia coli* Nissle 1917 (EcN) is renowned for its antimicrobial attributes, regulation of gut microbiota, and facultative anaerobic nature. As the cornerstone of the Mutaflor® drug, it has been utilized in the treatment of inflammatory bowel disease and gastrointestinal tumors[49–51]. However, bacterial therapy has been hindered by dose-dependent toxicity and the need for careful dosage control, which can compromise therapeutic efficacy[37,39]. Consequently, relying solely on bacteria to suppress tumors often fails to achieve the desired therapeutic outcomes[52]. Therefore, combining AIEgens with bacteria offers a promising solution by enhancing tumor targeting and enabling controlled release of therapeutic agents, ultimately improving the efficacy of cancer treatment while minimizing side effects[53].

In this work, we propose an innovative concept of an "AIEgen Bacteria Hybrid Bionic Robot" (EcN@INX-2) that integrates AIEgen with EcN to achieve multimodal phototherapeutic outcomes (Fig. 1). By strategically modulating the molecular structure of AIEgen, we successfully synthesized INX-$PF6^-$ (INX-2), which exhibits AIE characteristics, NIR absorption, NIR-II emission, remarkable photothermal and photoacoustic properties. Furthermore, EcN@INX-2 combines these unique properties with the tumor-targeting capabilities of EcN. Upon intravenous administration, the hybrid bionic robot preferentially localize within tumor tissues due to the natural hypoxia-targeting ability of EcN. In vivo multimodal imaging facilitates discernment between tumors and normal tissues with high sensitivity, thereby enabling precise targeting of tumor treatments. The light-induced generation of ROS through PDT further promotes ICD in tumor cells, potentiating anti-tumor immune responses. This study seamlessly integrates robotics with biological systems, imbuing EcN bacteria with phototheranostic AIEgen properties to fabricate fully motile bio-hybrid microrobots. It underscores the potential of bacteria-mediated enhancement of anti-tumor immunotherapy through the deployment of phototheranostic AIEgen.

Results

Molecular design, synthesis and characterization

To construct a multimodal functional probe, INX-I^- (INX-1) and INX-$PF6^-$ (INX-2) were ingeniously fabricated by selecting bis(4-methoxyphenyl)amine, 2,3-dihydro-1H-xanthene and 1-ethyl-2,3,3-trimethyl-3H-indolium iodide as the strong donor, π-bridge, and acceptor, respectively. The iodide (I^-) and hexafluorophosphate ($PF6^-$) were introduced into the molecules as counter ions, which are expected to regulate the solubility and luminescence properties at the aggregated. The propeller-like twisted structures of INX-1 and INX-2 could not only efficaciously restrain the fluorescence quenching in intraparticle aggregates by significantly reducing the intermolecular π-π stacking, but also extend the intermolecular distance and induce relatively loose intermolecular packing in the aggregate state, which greatly helpful to reserve part of the intramolecular rotation, thus favoring heat generation within aggregate. These aforementioned structural features would endow INX-2 with typical aggregation-induced near-infrared second window fluorescence emission (NIR-II AIE) characteristics and equip the resulting AIE aggregate with prominent versatility (PDT and PTT) as well as longer absorption/emission wavelengths.

To verify the hypotheses, we initially designed and synthesized two PSs (namely INX-1 and INX-2, Fig. 2a and Supplementary Fig. 1). The details of synthesis information were shown in Supplementary Fig. 1. All of the intermediates and target compounds were smoothly obtained by a few reactions, and well confirmed by nuclear magnetic resonance (NMR) and high resolution mass spectra (HRMS) as shown in Supplementary Figs. 2–5. INX-1 and INX-2 were scrutinized for their absorption and emission characteristics through analysis of their UV-visible-near infrared (UV-NIR) and photoluminescence (PL) spectra. Figure 2b illustrates that both INX-1 and INX-2 exhibited extended absorption wavelengths. Notably, INX-2 showed elongated emission wavelengths with a portion of its emission spectrum in the near-infrared region (NIR-II window), thereby facilitating its applicability in NIR-II fluorescence imaging (Fig. 2c). Consequently, INX-2 was chosen for subsequent experimentation. Subsequently, the AIE characteristics of INX-2 were scrutinized by monitoring its fluorescence in a dimethyl sulfoxide (DMSO)/Toluene mixed solvents with varying toluene fractions ($f_{Toluene}$). It was observed that INX-2 manifested weak fluorescence in pure DMSO solvent, with its fluorescence gradually intensifying as the toluene fraction increased (Supplementary Figs. 6a, b), signifying its favorable propensity towards AIE.

Subsequently, an exploration into the photothermal effects of INX-2 was undertaken. As depicted in Fig. 2d and Supplementary Fig. 7, the temperature escalated proportionally with the increase in INX-2 concentration under laser irradiation (660 nm, 0.45 W cm^{-2}, 5 min), accompanied by a photothermal conversion efficiency (η) of 46.26% (Fig. 2e). The PA spectra were measured by assessing the intensity across various wavelengths ranging from 680 nm to 970 nm, unveiling a robust photoacoustic signal of INX-2 at 735 nm (Fig. 2f). To assess the ROS generation capability of INX-2, theoretical calculations were executed utilizing density functional theory (DFT) and time-dependent

https://doi.org/10.1038/s41467-025-57533-y

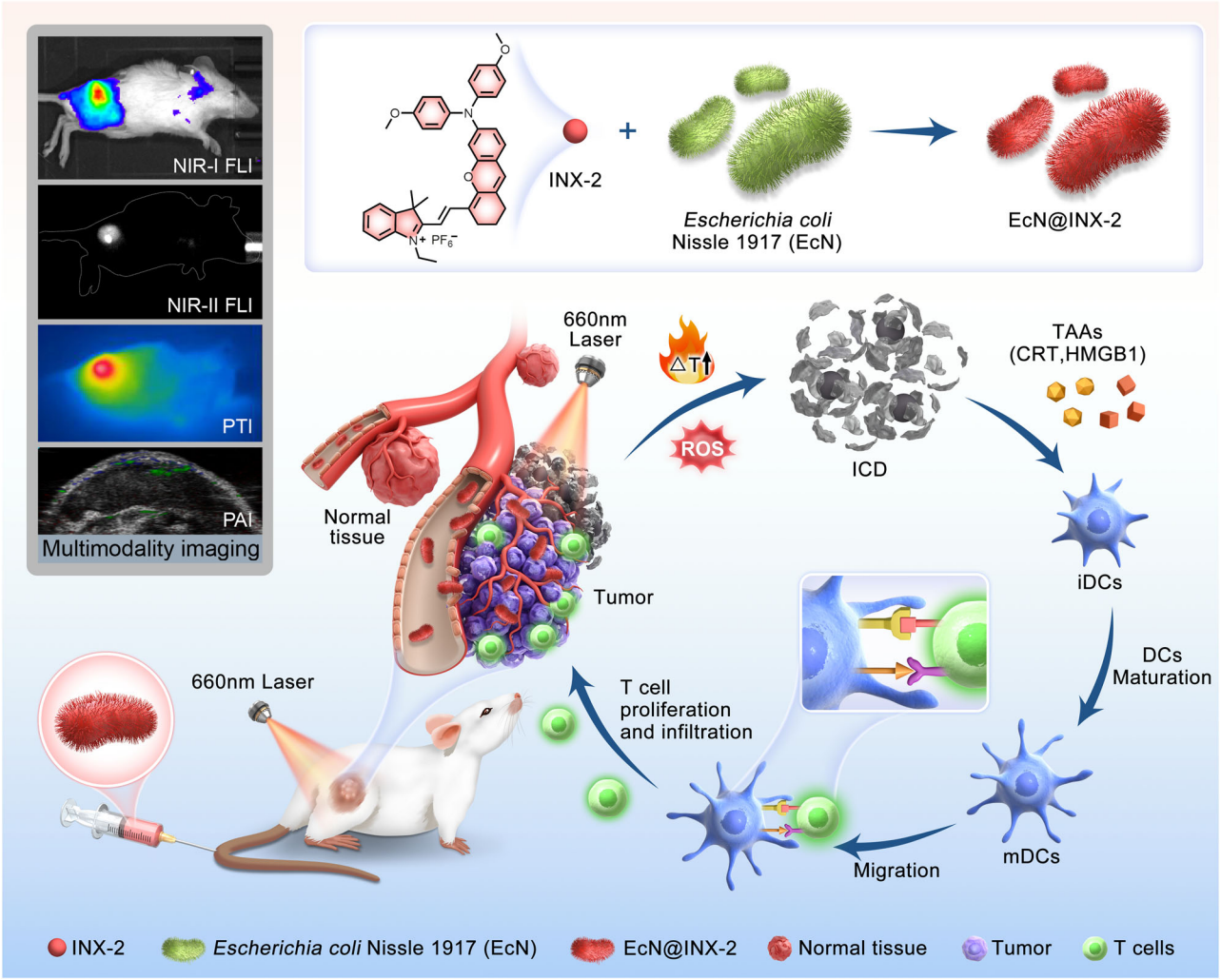

Fig. 1 | Schematic illustrative depiction of the AIEgen bacteria hybrid bionic robot EcN@INX-2 for guiding multimodal imaging and its application in elucidating cancer immunotherapy mechanisms. An AIEgen bacteria hybrid bionic robot, EcN@INX-2, was fabricated by integrating the AIEgen (INX-2) with bacteria (EcN). Following systemic administration, EcN@INX-2 infiltrates the tumor site with its intrinsic tumor-targeting ability to facilitate multimodal imaging. Laser irradiation of the tumor for combined photodynamic and photothermal therapy induces ICD, triggers activation of $CD4^+$ and $CD8^+$ T cells, and elicits a potent immune response, resulting in significant anti-tumor efficacy.

density functional theory (TD-DFT) with Gaussian 09 program at BYLYP/6-31 G(d, p) level[54,55]. The energy differential of 2.23 eV between the highest occupied molecular orbital (HOMO) and the lowest unoccupied molecular orbital (LUMO) of INX-2 was ascertained (Fig. 2g), facilitating the proficient intersystem crossing (ISC) of ROS from oxygen molecules[56]. The distribution of HOMO and LUMO orbitals of INX-2 is significantly different due to the donor-acceptor (D-A) structure. This results in INX-2 having a $\Delta E_{S1\text{-}T1}$ value as small as 0.681 eV (Figs. 2h, Table S1). Furthermore, the computed SOC value between S_1 and T_1 of INX-2 stood at 0.09 cm^{-1}. The relatively low $\Delta E_{S1\text{-}T1}$ and moderate SOC values are expected to promote T_1 state formation via effective ISC, which reveals the great potential of INX-2 to produce ROS efficiently, for either type-I electron transfer or type-II energy transferred processes. However, the energy gap, $\Delta E_{S0\text{-}T1}$, is lower than the triplet oxygen ($^3O_2$) / singlet oxygen ($^1O_2$) band gap, thereby precluding type-II energy transfer processes[57]. This theoretical prediction is consistent with the experimental validation of reactive ROS types produced by INX-2. In addition, we further verified that the single electron transfer could take place between excited INX-2 and the environmental hydroxyl anion before INX-2 transfers electrons to O_2. The entire process was accompanied by a Gibbs free energy change of -14.32 kcal. mol^{-1}, calculated by PWPB95-D3/def2-TZVP method using the ORCA 4.2.1 program (Supplementary Figs. 8, Table S2–5). In summary, the theoretical calculations conducted via computational software delineated notable photodynamic activity of INX-2.

ROS can be categorized as type-I and type-II based on the distinct mechanisms of interaction between PS and oxygen[58,59]. Triplet state PS generates type-I ROS through electron transfer, primarily involving superoxide anion radical ($O_2^{\cdot-}$), hydrogen peroxide (H_2O_2), and hydroxyl radical (·OH). In contrast, type-II ROS mainly consist of $^1O_2$ produced by oxygen through energy transfer (Fig. 3a). The capacity of INX-2 to produce ROS through laser stimulation in aggregate state (DMSO/phosphate-buffered saline (PBS), 1/99, v/v) was further investigated using a fluorescent probe to detect ROS. The overall ROS generation ability of INX-2 was initially evaluated using the commercial 2′,7′-dichlorodihydrofluorescein diacetate (DCFH-DA) as a comprehensive ROS indicator[60]. When the combination of DCFH and PS was exposed to a laser (660 nm, 0.45 W cm^{-2}, 10 min), the fluorescence intensity of the oxidized product DCF at 525 nm exhibited a notable increase. In particular, in comparison to the initial fluorescence intensity, the fluorescence intensity of the commercial PS Chlorin e6 (Ce6), and INX-2 rose by 100-fold, and 550-fold respectively (Fig. 3b). Various reactive oxygen fluorescent probes were utilized to elucidate the specific ROS produced by INX-2 under a laser (660 nm,

https://doi.org/10.1038/s41467-025-57533-y

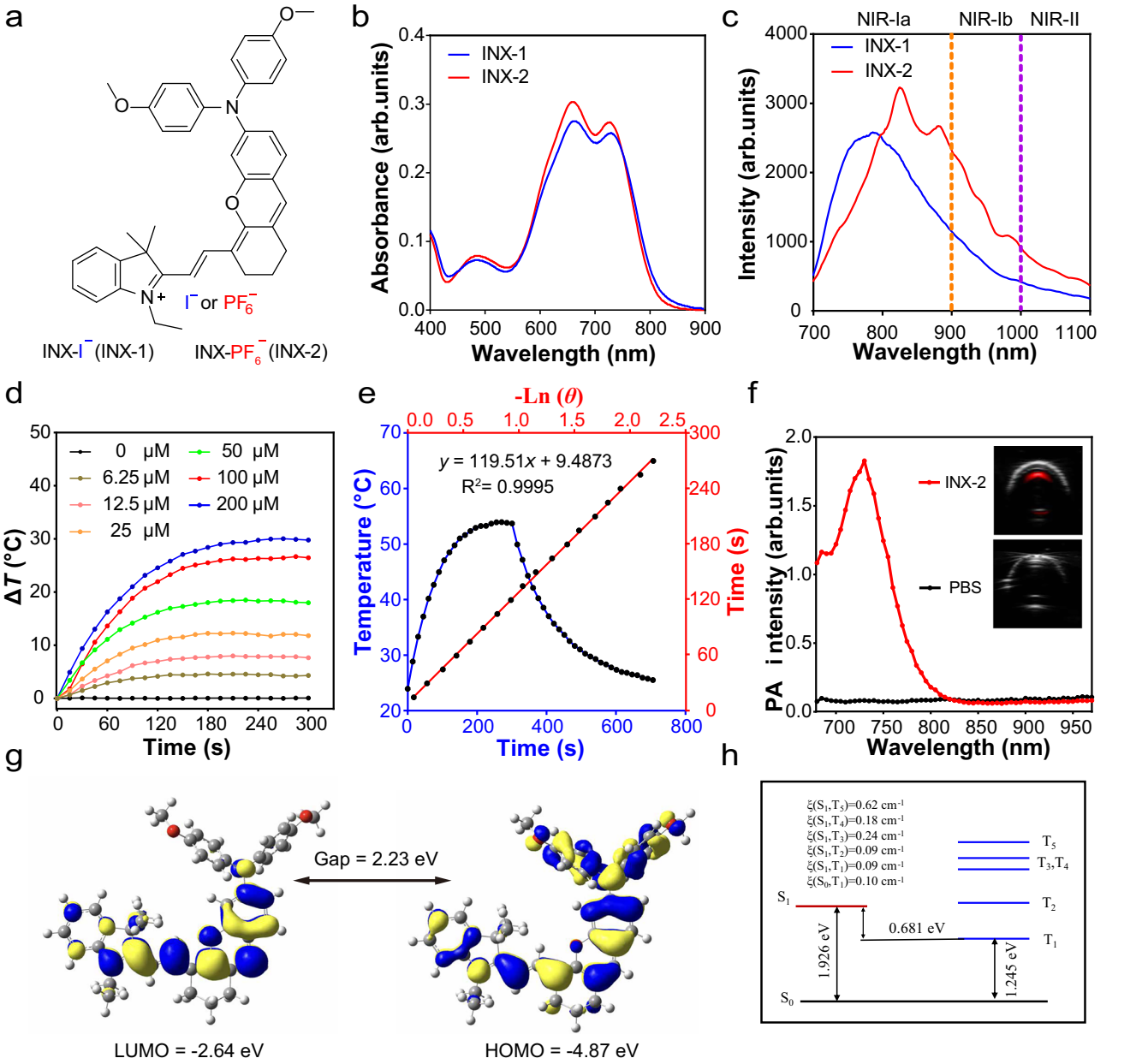

Fig. 2 | Physical and photophysical characterization of AIEgen. a The molecular chemical structure of INX-1 (INX-I^-) and INX-2 (INX-PF_6^-). **b** The absorption spectra of INX-1 and INX-2 in H_2O/DMSO (99% H_2O) solution. **c** The PL spectra of INX-1 and INX-2 in H_2O/DMSO (99% H_2O) solution. **d** Temperature difference (ΔT) of various concentrations of INX-2 under laser irradiation (660 nm, 0.45 W cm^{-2}, 5 min) over time. **e** The temperature profile of INX-2 reached a stabilized temperature under laser irradiation (660 nm, 0.45 W cm^{-2}, 5 min), followed by laser deactivation for cooling (black line). Linear temporal data versus the negative natural logarithm of the attained temperature during the cooling phase (red line) were plotted. **f** Photoacoustic (PA) spectra of INX-2. **g** Calculated INX-2 molecular geometry, highest occupied molecular orbital (HOMO), lowest unoccupied molecular orbital (LUMO), and energy levels. **h** Schematic depiction of the intersystem crossing (ISC) transition of INX-2. For (**b**–**h**), experiment was repeated three times independently with similar results. Source data are provided as a Source Data file.

0.45 W cm^{-2}, 10 min) (Fig. 3c–f). Singlet oxygen sensor green (SOSG) and 9,10-anthracenediylbis (methylene) dipropanedioic acid (ABDA) were used for the detection of $^1O_2$, hydroxyphenyl fluorescein (HPF) was employed for the identification of ·OH, and dihydrorhodamine 123 (DHR123) was deployed for the detection of $O_2^{\cdot-}$ The results revealed that the fluorescence intensity of the mixed solution of Ce6 with SOSG exhibited a rapid initial surge under laser irradiation (660 nm, 0.45 W cm^{-2}, 10 min). Contrariwise, only a weak change in the fluorescence SOSG intensity was observed upon exposure to INX-2 under identical circumstances (Fig. 3c). Similarly, the absorption peaks of ABDA exhibited a gradual decline in the presence of Ce6, while there was only a weak decrease in the absorption peaks of ABDA when subjected to INX-2 under the same conditions (Fig. 3d). The fluorescence intensities of both SOSG and ABDA suggested that INX-2 produced only a very small amount of $^1O_2$ in the solution. Conversely, in the presence of INX-2, the fluorescence intensities of HPF at 525 nm and DHR123 at 525 nm exhibited significant augmentation, with a 23.8-fold amplification in the fluorescence intensity of HPF (Fig. 3e) and a 14.7-fold enhancement in the fluorescence intensity of DHR123 (Fig. 3f). These observations indicate that INX-2 possesses the capability to generate ·OH and $O_2^{\cdot-}$ in the solution. The experimental results were consistent with the theoretical calculation results (Fig. 2g, h and Supplementary Figs. 8). Electron spin resonance (ESR) spectroscopy, performed by irradiating mixtures containing 4-amino-

https://doi.org/10.1038/s41467-025-57533-y

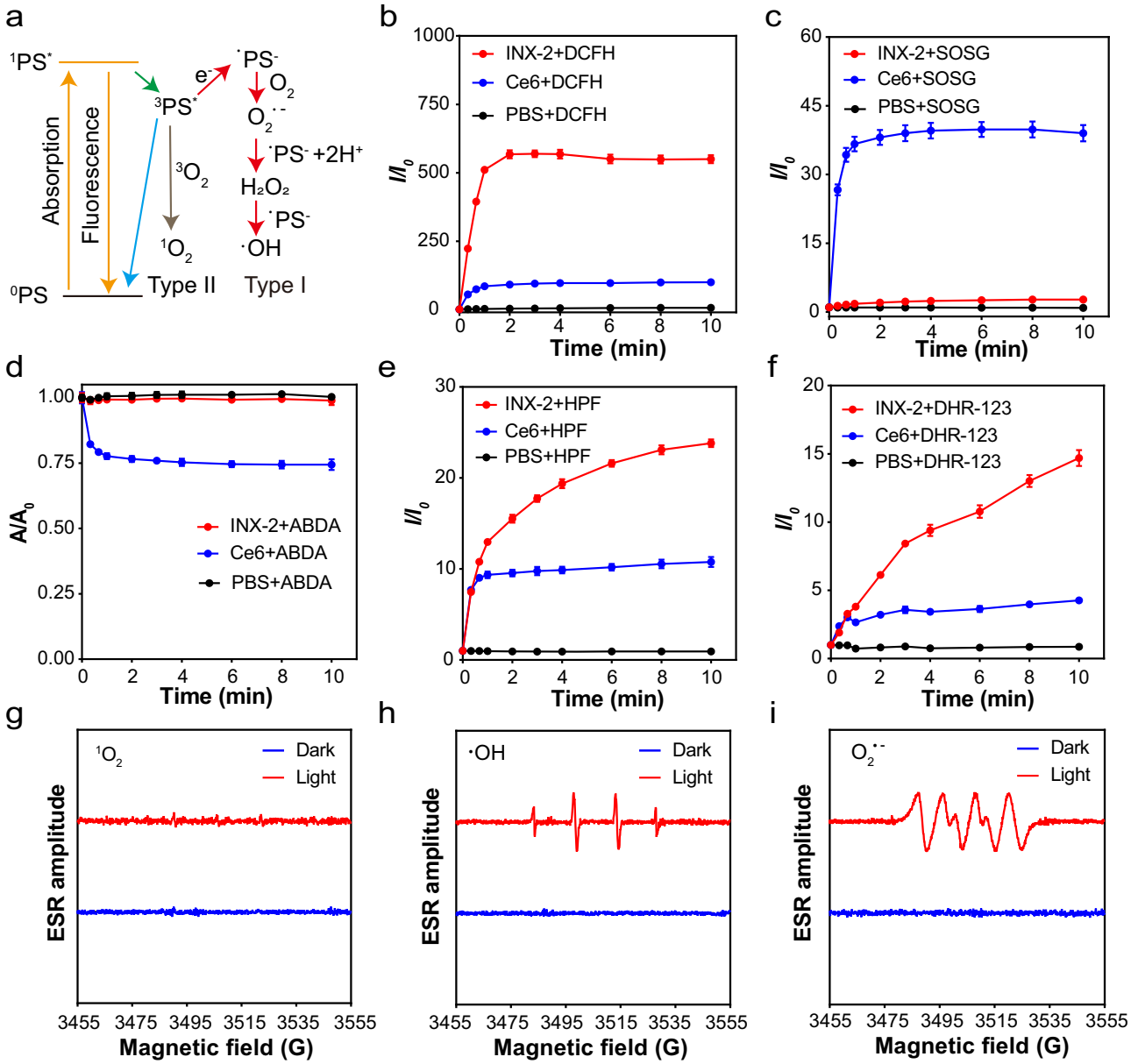

Fig. 3 | Determination of reactive oxygen species (ROS) types produced by INX-2. a Schematic diagram of photodynamic therapy based on Jablonski. **b** ROS produced by INX-2 after laser irradiation (660 nm, 0.45 W cm^{-2}, 10 min) using 2,7-Dichlorodihydrofluorescein diacetate (DCFH-DA) as an indicator. ($n = 3$ independent samples). **c** Relative changes in fluorescence intensity of singlet oxygen sensor green (SOSG) or (**d**) absorption intensity of 9,10-anthracenediylbis (methylene) dipropanedioic acid (ABDA) decomposition after laser irradiation (660 nm, 0.45 W cm^{-2}, 10 min) in the presence of different photosensitizers. ($n = 3$ independent samples). **e** Changes in fluorescence intensity of hydroxyphenyl fluorescein (HPF) and (**f**) dihydrorhodamine 123 (DHR-123) with time during laser irradiation (660 nm, 0.45 W cm^{-2}, 10 min) in the presence of different photosensitizers. ($n = 3$ independent samples). **g**–**i** Electron spin resonance (ESR) signals of 4-amino-2,2,6,6-tetramethylpiperidine (TEMP) or 5,5-dimethyl-1-pyrroline-oxide (DMPO) in the presence of INX-2 for characterization of $^1O_2$ (**g**), ·OH (**h**) and $O_2^{\cdot-}$ (**i**) during xenon lamp irradiation (300 W cm^{-2}, 5 min). I_0 and I represent the fluorescence or absorbance intensities of the fluorescent probe before and after laser irradiation (660 nm, 0.45 W cm^{-2}, 10 min), while A_0 and A are the absorbance intensities under the same conditions. Data are presented as mean ± SD ($n = 3$ independent samples). For **g**–**i** experiment was repeated three times independently with similar results. Source data are provided as a Source Data file.

2,2,6,6-tetramethylpiperidine (TEMP) or 5,5-dimethyl-1-pyrroline-oxide (DMPO), corroborated that INX-2 barely produces $^1O_2$ under xenon lamp irradiation (300 W cm^{-2}, 5 min) (Fig. 3g), but yielded a substantial quantity of ·OH (Fig. 3h) and $O_2^{\cdot-}$ (Fig. 3i), aligning with the aforementioned results obtained with the ROS fluorescent probe. Based on the aforementioned experimental validation, INX-2 predominantly generates type-I ROS compared to Ce6 (Supplementary Fig. 9), thereby enabling optimal utilization of limited oxygen. Consequently, INX-2 presents notable advantages in the treatment of solid tumors.

AIEgen bacteria hybrid bionic robot

Bacteria exhibit a remarkable capacity to colonize tumors, owing to the intrinsic characteristics of hypoxia and diminished immune surveillance within the tumor microenvironment. Moreover, these microorganisms have a propensity to flourish in such hypoxic and immunosuppressive conditions, rendering them ideal candidates as delivery vehicles for tumor-targeted therapies. In this investigation, we employed the probiotic EcN as a vector for INX-2 delivery. Confocal laser scanning microscopy (CLSM) images revealed that INX-2 molecules localized in the cytosol and on the surface of the bacteria after

https://doi.org/10.1038/s41467-025-57533-y

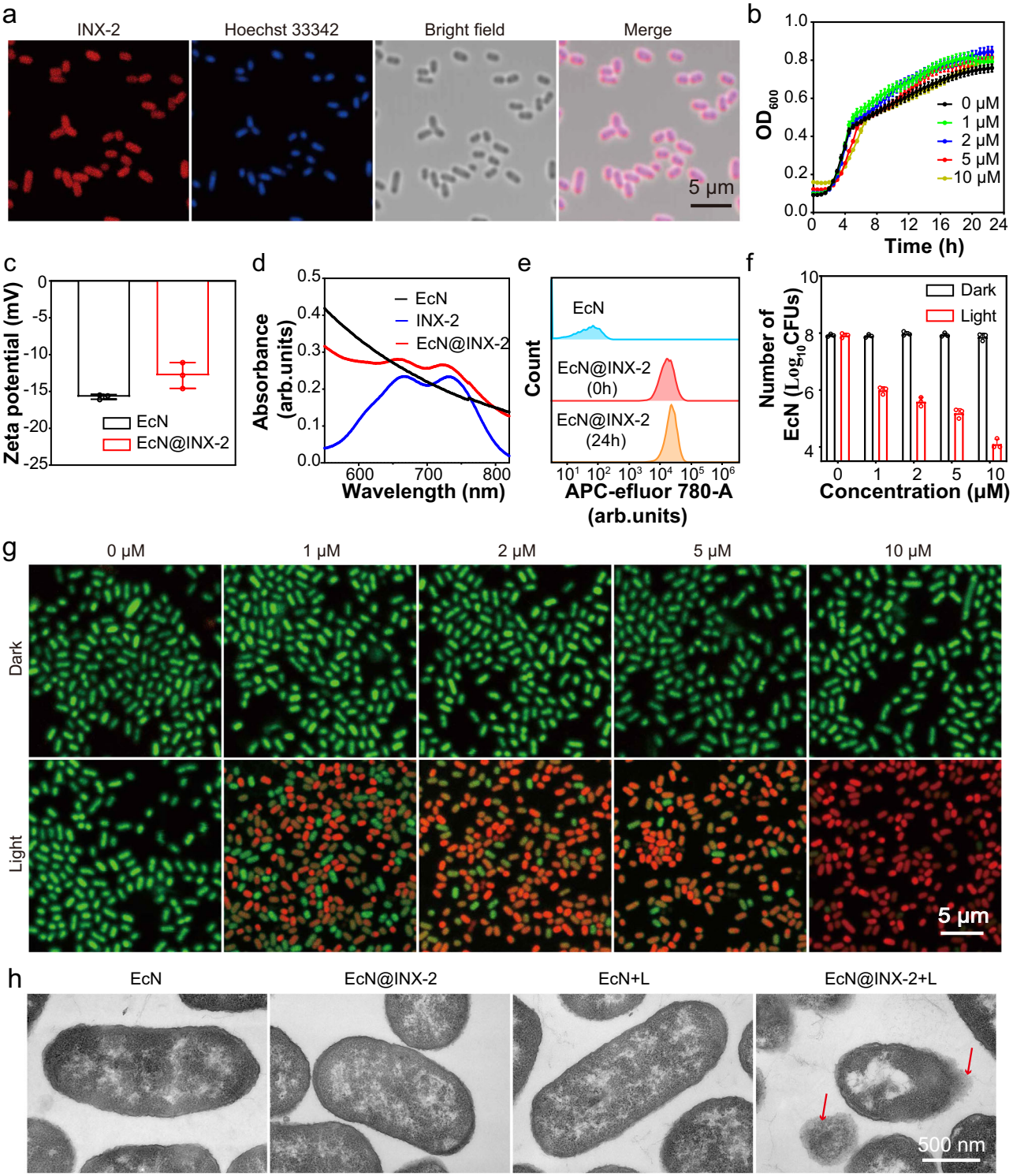

Fig. 4 | Characterization of EcN after electrostatic adsorption of INX-2. **a** Representative CLSM images of EcN labeled with INX-2 (red fluorescence) and Hoechst 33342 (blue fluorescence). (Scale bar: 5 μm). **b** Growth curves of EcN in LB supplemented with varying concentrations of INX-2 at 37 °C ($n = 6$ independent samples). **c** Zeta potential of EcN and EcN@INX-2 ($n = 3$ independent samples). **d** Absorption spectra of EcN, INX-2 and EcN@INX-2. **e** Representative flow cytometry histograms showing the fluorescence of EcN loaded with INX-2 at various time points. **f** Number of colonies after incubation with different concentrations of INX-2 in bacterial suspensions incubated with laser irradiation (660 nm, 0.45 W cm^{-2}, 10 min) and then coated on LB agar plates ($n = 3$ independent samples). **g** Representative CLSM images depicting EcN co-cultured with the INX-2 complex following either in darkness or under laser irradiation (660 nm, 0.45 W cm^{-2}, 10 min), utilizing double fluorescence staining with SYTO 9 (green fluorescence) and PI (red fluorescence) (Scale bar: 5 μm). **h** Representative TEM images depicting the morphological characteristics of EcN following incubation with or without INX-2 under dark conditions, as well as post laser irradiation (660 nm, 0.45 W cm^{-2}, 10 min), disrupted bacterial walls are denoted by red arrows (Scale bar: 500 nm). Data are presented as mean ± SD ($n = 3$ independent samples). For **a**, **d**, **e**, **g**, and **h** the experiment was repeated three times independently with similar results. Source data are provided as a Source Data file.

30 min of coincubation with EcN (Fig. 4a). Ensuring the vitality of bacteria represents a pivotal concern when harnessing them as conveyors of therapeutic agents. The growth dynamics of EcN in a liquid medium were scrutinized through the evaluation of optical density (OD) at 600 nm, serving as a measure of the opaqueness of cell suspension. Examination of the growth profiles unveiled that the INX-2-modified EcN bacteria (EcN@INX-2) demonstrated typical proliferation and division attributes, with a marginally discernible disparity in viability between the EcN and EcN@INX-2 (Fig. 4b). The Zeta potential of EcN@INX-2 was determined to be −12.83 ± 1.75 mV, slightly less negative than that of EcN at −15.73 ± 0.32 mV (Fig. 4c). This variance may be ascribed to the effective surface modification of EcN with the positively charged INX-2. Evaluation of UV absorption spectroscopy unveiled that EcN@INX-2 exhibited identical characteristic absorption peaks as INX-2 (Fig. 4d), signifying that INX-2 had adhered and encapsulated to EcN. Fluorescence signals emanating from INX-2 molecules affixed to the bacterial surface at various intervals of time were discerned via flow cytometry. It was noted that the fluorescence intensity remained unaltered after 24 h of co-incubation, indicating a stable binding of INX-2 to the bacteria (Fig. 4e). These findings collectively imply that INX-2 adheres to bacteria through electrostatic adsorption to successfully form a stable AIEgen bacteria bionic robot EcN@INX-2. In order to quantitatively characterize the loading capacity of a single EcN on INX-2, we constructed a standard curve (Supplementary Fig. 10) and calculated that the loading capacity of a single bacterium for molecules was 0.146 pg and the loading efficiency was 96.7%. Moreover, EcN@INX-2 was washed three times with water and was still able to maintain binding stability (Supplementary Figs. 11a, b). The results observed that ROS release and photothermal performance of EcN@INX-2 slightly decreased after INX-2 was combined with EcN (Supplementary Figs. 12a, b). Moreover, despite the dilution of INX-2 concentration in individual bacteria with each cell division, the collective photothermal effect of the entire bacterial culture remained comparable to its initial state (Supplementary Fig. 12b). This finding indicated that, despite the dilution effect, the collective photothermal response of the bacterial population is maintained.

To evaluate the potential antimicrobial efficacy of INX-2, we investigated its direct interaction with bacterial cells. As shown in Fig. 4f and Supplementary Fig. 13, bacterial suspensions derived from distinct treatments were cultured on Luria Bertani (LB) agar and incubated for a duration for 24 h. Following this, colony counts were recorded to ascertain the extent of bacterial proliferation. In the absence of laser irradiation, bacterial growth remained unaltered. However, upon exposure to laser irradiation (660 nm, 0.45 W cm^{-2}, 10 min), a conspicuous reduction in bacterial population was observed (Fig. 4f). To further substantiate the bactericidal functionality of INX-2, we performed bacterial viability assays employing SYTO 9 green and propidium iodide (PI) red fluorescent nucleic acid dye. The acquired data revealed a dose-dependent escalation in the number of dead EcN cells under laser irradiation (660 nm, 0.45 W cm^{-2}, 10 min), thereby corroborating the antimicrobial potential of INX-2 (Fig. 4g). Notably, transmission electron microscopy (TEM) images elucidated that the morphology of EcN remained unaltered both before and after the adsorption of INX-2. However, under laser irradiation (660 nm, 0.45 W cm^{-2}, 10 min), the cell walls and membranes of the INX-2-loaded EcN exhibited membrane structural membrane collapse (Fig. 4h).

Evaluation of AIEgen bacteria hybrid bionic robot in vitro

Based on the excellent photodynamic and photothermal properties of INX-2, the in vitro anti-tumor effect of EcN@INX-2 has been validated. Cell viability was evaluated using the conventional 3-(4,5-dimethylthiazol-2-yl)-2,5-diphenyltetrazolium bromide (MTT) assay. CT26 cells were co-incubated with varying concentrations of EcN@INX-2, subsequently exposed to laser irradiation (660 nm, 0.45 W cm^{-2}, 10 min) or maintained under dark conditions. Notably, the EcN@INX-2 + L group demonstrated pronounced cytotoxicity towards CT26 cells, with cell viability displaying a concentration-dependent decrease (Supplementary Fig. 14). It has been demonstrated that PDT-induced ROS and PTT-mediated tumor injury can trigger an ICD cascade, thereby enhancing tumor susceptibility to immunotherapy[61,62]. Accordingly, we investigated the capability of the EcN@INX-2 + L group to induce ICD in vitro. Immunofluorescence imaging revealed that the EcN@INX-2 + L group significantly promoted surface-exposed calreticulin (ecto-CRT) exposure on cancer cells compared to both the PBS group and the laser-irradiated group (Fig. 5a). In addition, the fluorescence intensity of high mobility group protein B1 (HMGB1) in the nucleus was significantly reduced in the EcN@INX-2 + L group compared with that in the control group, suggesting that the treatment in the EcN@INX-2 + L group promoted the release of HMGB1 from the nucleus (Figs. 5b, Supplementary Fig. 15). The findings indicated that treatment of CT26 cells with EcN@INX-2 + L resulted in a pronounced increase in ecto-CRT expression and a significant reduction in HMGB1 expression, corroborating the CLSM observations. These results suggest that EcN@INX-2 + L can effectively induce ICD in tumor cells, which is pivotal for enhancing tumor antigen presentation and T lymphocyte activation.

Building on the promising outcomes of the in vitro experiments, we extended our investigation to evaluate the tumor penetration and cytotoxicity of EcN@INX-2 using a 3D spheroid model of CT26 cells. The 3D tumor spheroids were subjected to individual treatments with INX-2 and EcN@INX-2 for 12 h, followed by Z-stack scanning via CLSM. The results indicated that treatment with free INX-2 resulted in a red fluorescent signal predominantly locating on the surface of the spheroids. In contrast, fluorescence was detected within the inner layers of the tumor spheroids upon treatment with EcN@INX-2, demonstrating enhanced permeability of INX-2 facilitated by EcN (Fig. 5c, d). This observation underscores the potential of the AIEgen bacteria hybrid bionic robot for improving therapeutic effects in deep tumor tissues. Following 12 h of incubation with the respective formulations, the 3D tumor spheroids were irradiated witha laser (660 nm, 0.45 W cm^{-2}, 10 min). Cell viability within the spheroids was evaluated using the LIVE/DEAD Viability/Cytotoxicity Assay Kit. Notably, the 3D tumor spheroids treated with EcN@INX-2 + L had extensive cell death throughout the spheroids, including the inner regions (Fig. 5e). Conversely, the treatment with INX-2 + L induced cell death primarily restricted to the outermost layer of the spheroids. The treatments with PBS, PBS + L, INX-2 and EcN@INX-2 showed minimal impact on cell viability. These results indicate that EcN@INX-2 possesses the capability to penetrate the core regions of 3D tumor spheroids, effectively eradicating hypoxic regions and ablating CT26 cells under laser irradiation (660 nm, 0.45 W cm^{-2}, 10 min).

In vivo biodistribution of EcN

To assess the accumulation of EcN in the female mouse CT26 subcutaneous tumor model, a long-term observation of the in vivo biodistribution of EcN after injection was performed. A sterile collection of tissues from key organs (heart, liver, spleen, lungs and kidneys) and mouse tumors were performed before EcN injection into the tail vein (day 0) and at specified intervals post-injection (day 1, 3, 6, 10 and 16). The tissues were then homogenized, diluted into gradient suspensions with PBS, and plated on LB agar to enumerate bacterial colonies. Following systemic drug administration via the tail vein, the bacteria were distributed in both the tumor and different organ tissues. Importantly, the initial bacterial colony count in the tumor and other major organs was similar on day 1. However, after 3 days, a significantly greater proliferation of colonies occurred in the tumor compared to the other major organs. Over time, bacterial colonies in the organs gradually decreased and were eventually cleared by the immune system. Conversely, colonies in tumor tissues persisted for up to 16 days, further confirming the ability of EcN to selectively target tumor regions owing to its intrinsic hypoxic tropism affinity (Supplementary Fig. 16).

https://doi.org/10.1038/s41467-025-57533-y

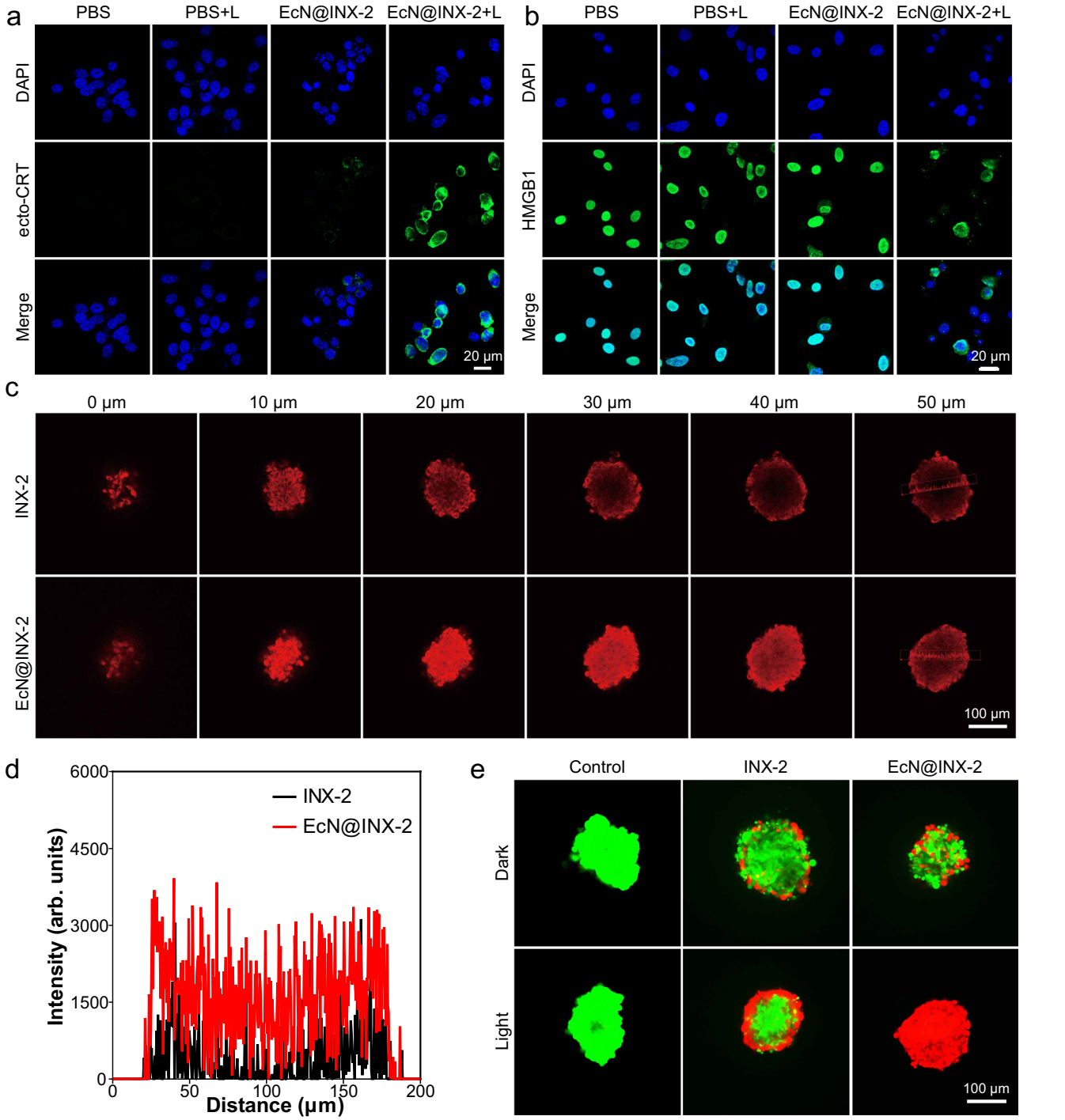

Fig. 5 | Application of EcN@INX-2 at the CT26 cells and 3D tumor level. **a** Representative immunofluorescence images showing ecto-CRT (green fluorescence) exposure on the surface of CT26 cells under various treatments. The cell nuclei were stained with DAPI (blue fluorescence). (Scale bar: 20 μm). **b** Representative immunofluorescence images showing reduced HMGB1 (green fluorescence) in the nucleus of CT26 cells following various treatments. The cell nuclei were stained with DAPI (blue fluorescence). (Scale bar: 20 μm). **c** CLSM images were captured spanning from the surface to the center of the CT26 tumor spheroid using a Z-stack thickness of 10 μm. The red fluorescence indicates INX-2. (Scale bar: 100 μm). **d** Histogram depicting the fluorescence intensity profile of a CT26 3D tumor sphere in panel (**c**) at a depth of 50 μm. **e** Representative CLSM images showing CT26 3D tumor spheroids co-stained with calcein-AM (green fluorescence) and propidium iodide (red fluorescence) (Scale bar: 100 μm). For **a**–**e**, experiment was repeated three times independently with similar results. Source data are provided as a Source Data file.

Multimodality imaging of tumors in vivo

The in vitro experiments showed significant efficacy of EcN@INX-2 on 3D tumor spheroids, and the in vivo experiments in female mice confirmed that EcN was able to selectively target hypoxic regions of tumors while exhibiting durable retention ability. Subsequently, a CT26 tumor female mouse model was constructed, and the precise accumulation of EcN@INX-2 at the tumor site in vivo was evaluated using multiple imaging techniques after EcN@INX-2 was injected via the tail vein when the tumor volume reached 200 mm^3. Given that INX-2 emits fluorescence in both the NIR-I and NIR-II windows, the

https://doi.org/10.1038/s41467-025-57533-y

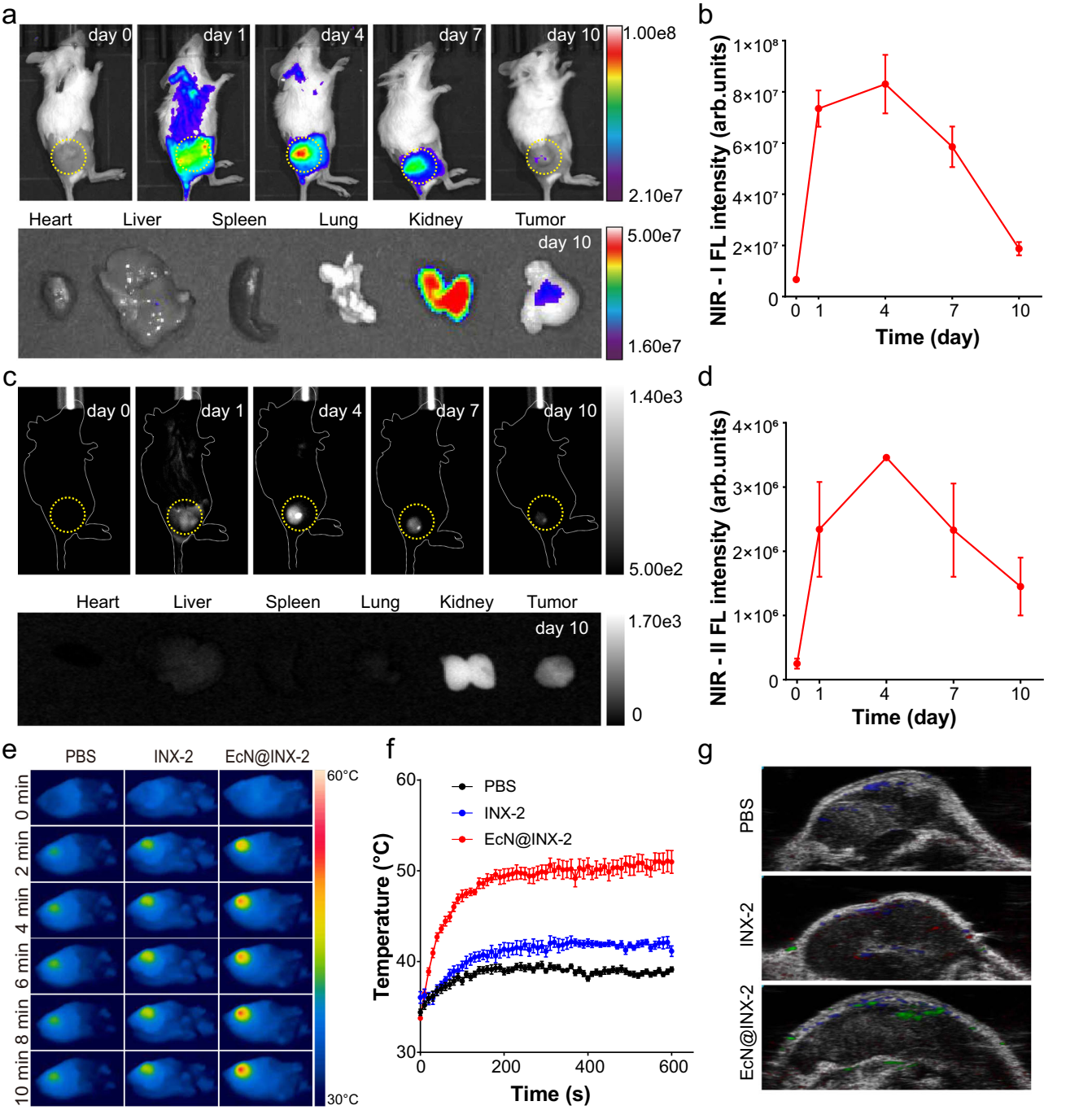

Fig. 6 | Multimodal imaging of EcN@INX-2 in CT26 tumor-bearing female mice. **a** Representative NIR-I fluorescence imaging of tumor sites in female mice at different times after intravenous injection of EcN@INX-2 as well as of major tissue organs and tumor tissues isolated at day 10. Yellow circle denote the tumor. **b** Quantitative analysis of the NIR-I fluorescence intensity of the tumor tissue in panel (**a**). ($n = 3$ mice). **c** Representative NIR-II fluorescence imaging of tumor sites in mice at different times after intravenous injection of EcN@INX-2 as well as of major tissue organs and tumor tissues isolated at day 10. Yellow circle denote the tumor. **d** Quantitative analysis of the NIR-II fluorescence intensity of the tumor tissue in panel (**c**) ($n = 3$ mice). **e** Representative photothermal imaging of mouse tumor tissue under laser irradiation (660 nm, 0.45 W cm^{-2}, 10 min) 1 day after tail vein injection of PBS, free INX-2 and EcN@INX-2. **f** Temperature variations of tumors in panel (**e**) after exposure to laser irradiation (660 nm, 0.45 W cm^{-2}, 10 min). ($n = 3$ mice). **g** Representative PA images of tumor tissues at 1 day after administration of EcN@INX-2 (After spectral separation, Blue represents deoxyhemoglobin, red represents oxyhemoglobin and green represents INX-2). Data are presented as mean ± SD ($n = 3$ mice). For (**a**, **c**, **e** and **g**), experiment was repeated three times independently with similar results. Source data are provided as a Source Data file.

observation of NIR-I and NIR-II fluorescence signals was also performed in the tumor-bearing female mice (Fig. 6 a,b,c,d). Both NIR-I and NIR-II fluorescence images distinctly depicted EcN@INX-2 localization within the tumor tissues, demonstrating dynamic changes in fluorescence intensity over 10 days, thus confirming substantial accumulation and retention of EcN@INX-2 in the tumor tissue. Thermal imaging was employed to observe tumor regions in female mice subjected to laser irradiation (660 nm, 0.45 W cm^{-2}, 10 min), with real-time infrared images directly depicting local temperature fluctuations (Fig. 6e). In the PBS-treated control group, tumor temperatures rose

https://doi.org/10.1038/s41467-025-57533-y

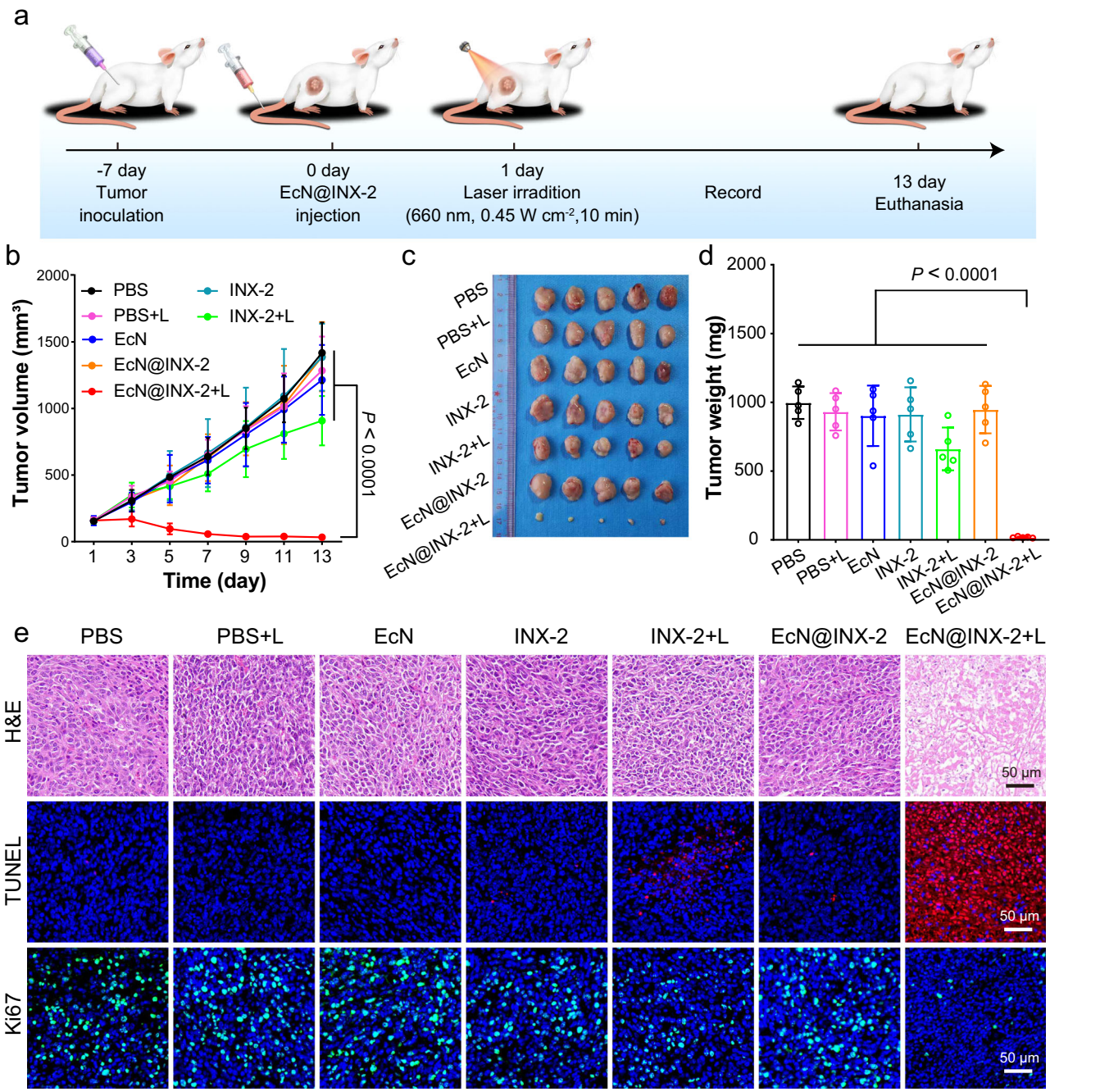

Fig. 7 | In vivo therapeutic evaluation of phototherapy mediated by EcN@INX-2. a Schematic diagram of the flow of in vivo treatment experiments in female mice. **b** The changes in tumor volume in different treatment groups during the treatment cycle ($n = 5$ mice). **c** Digital photographs of tumor tissue and tumor weight (**d**) from each group at the end of treatment observation ($n = 5$ mice). **e** Representative H&E and immunofluorescence staining of TUNEL (red fluorescence) and Ki-67 (green fluorescence) in tumor tissues following various treatments. The cell nuclei were stained with DAPI (blue fluorescence). (Scale bar: 50 μm). Data are presented as mean ± SD ($n = 5$ mice). For (**e**), experiment was repeated three times independently with similar results. For (**b** and **d**), statistical analyzes were performed using one-way ANOVA. Source data are provided as a Source Data file.

gradually and reached 39 °C under continuous laser irradiation (660 nm, 0.45 W cm^{-2}, 10 min), while in the free INX-2 administration group, temperatures at the tumor site reached 42 °C. By comparison, in the EcN@INX-2 group, tumor temperature reached 51 °C, highlighting the capability of EcN to facilitate targeted delivery of INX-2 to tumor tissue (Fig. 6f). To explore the photoacoustic effect of EcN@INX-2 in tumors, PA imaging at the tumor sites was conducted for the female mice received injections of PBS, EcN@INX-2 and equivalent free INX-2 1-day post-administration. Spectral separation techniques were applied to counteract the influence of hemoglobin and deoxyhemoglobin. The PA signal detected in the control group predominantly comprised hemoglobin (red) and deoxyhemoglobin (blue). Crucially, the EcN@INX-2 group exhibited a more prominent and darker PA signal (green) of INX-2 at the tumor site compared to the free INX-2 group, further affirming the tumor targeting and infiltration capabilities of EcN@INX-2 (Fig. 6g). In conclusion, the findings from fluorescence, photothermal and PA tri-modal imaging provide robust evidence affirming the tumor-targeted delivery, prolonged retention, and multimodal imaging functionalities of the AIEgen bacteria hybrid bionic robot EcN@INX-2.

https://doi.org/10.1038/s41467-025-57533-y

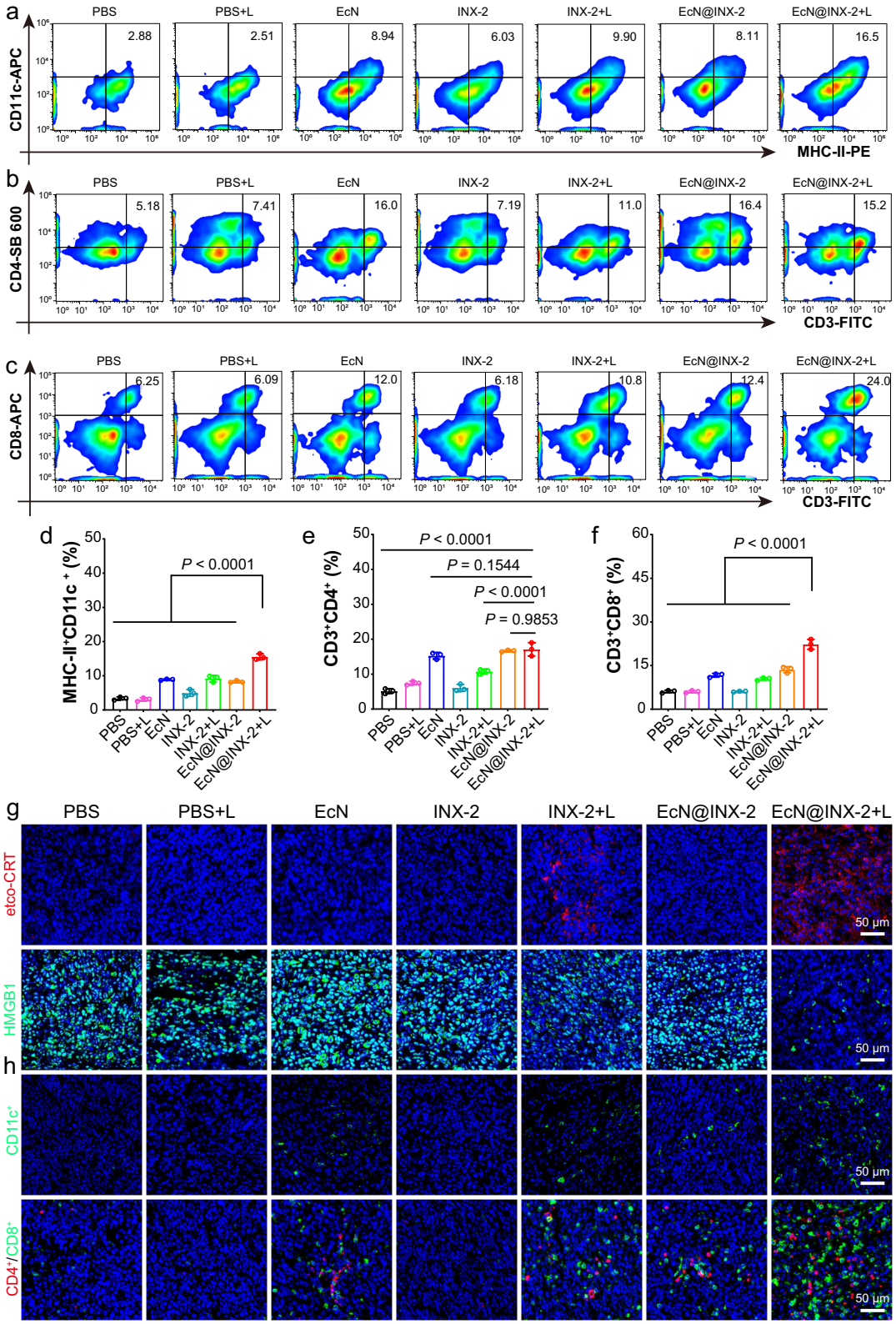

EcN@INX-2 in tumor treatment in vivo

Given the remarkable tumor-targeting ability of EcN@INX-2, the in vivo antitumor effect of EcN@INX-2 under laser irradiation after tail vein injection was further evaluated (Fig. 7a). CT26 tumor-bearing female mice were successfully established and randomly allocated to the following experimental cohorts: (I) PBS group; (II) PBS plus laser (PBS + L) group; (III) EcN group; (IV) INX-2 group; (V) INX-2 plus laser (INX-2 + L) group; (VI) EcN@INX-2 group; (VII) EcN@INX-2 plus laser (EcN@INX-2 + L) group. Laser irradiation (660 nm, 0.45 W cm^{-2}, 10 min) was performed 1 day after intravenous injection. Throughout the treatment regimen, the weight and tumor growth of each experimental group of mice were monitored every two day.

It could be observed that the tumor growth of the EcN@INX-2 + L group was significantly inhibited, and the average tumor volume at the

Fig. 8 | In vivo evaluation of photo-immunotherapy activation mediated by EcN@INX-2. a Representative flow cytometry plots depicting DCs maturation within tumor tissues following diverse treatments. **b** Representative flow cytometry plots depicting $CD3^+CD4^+$ helper T cells within tumor tissues following diverse treatments. **c** Representative flow cytometry plots depicting $CD3^+CD8^+$ cytotoxic T cells within tumor tissues following diverse treatments. **d** Quantitative analysis of flow cytometric results for mature DCs ($n = 3$ mice). **e** Quantitative analysis of flow cytometric results for $CD3^+CD4^+$ helper T cells ($n = 3$ mice). **f** Quantitative analysis of flow cytometric results for $CD3^+CD8^+$ cytotoxic T cells ($n = 3$ mice). **g** Representative CLSM captures of immunofluorescence staining depicting etco-CRT (red fluorescence) and HMGB1 (green fluorescence) on tumor sections from mice subjected to distinct treatment regimens. Nuclei (blue) were stained using DAPI. (Scale bar: 50 μm). **h** Representative CLSM captures of immunofluorescence staining depicting $CD11c^+$ DCs (green fluorescence), $CD4^+$ T (red fluorescence) and $CD8^+$ T (green fluorescence) cells on tumor sections from female mice subjected to distinct treatment regimens. Nuclei (blue fluorescence) were stained using DAPI. (Scale bar: 50 μm). Data are presented as mean ± SD ($n = 3$ mice). For (**d**, **e** and **f**), statistical analyzes were performed using one-way ANOVA. For (**a**, **b**, **c**, **g** and **f**), experiment was repeated three times independently with similar results. Source data are provided as a Source Data file.

end of the observation was only 33.83 mm^3, much smaller than that in the INX-2 + L group (908.31 mm^3) and the PBS group (1417.89 mm^3) (Figs. 7b, c and Supplementary Fig. 17). The average tumor mass observed after treatment in the EcN@INX-2 + L group was measured merely 18.38 mg (Fig. 7d), which was much smaller than that of the PBS group (937.286 mg). The excellent anti-tumor efficacy of the EcN@INX-2 + L group was mainly attributed to the targeting effect of EcN and the PDT and PTT of INX-2. Hematoxylin and eosin (H&E) staining as well as terminal deoxynucleotidyl transferase-mediated nick end labeling (TUNEL) assay further confirmed the pronounced antitumor effects of EcN@INX-2. H&E staining showed that among the different treatment groups, the most pronounced damage took place in the EcN@INX-2 + L group, with disappearance of nuclei and a light red cytoplasm (Fig. 7e, row 1). In addition, strong red fluorescence was observed in TUNEL staining, suggesting that EcN@INX-2 + L group induced apoptosis of tumor cells (Fig. 7e, row 2). Furthermore, Ki-67 antibody staining elucidated the proliferative dynamics of endogenous cell populations within malignant tumors and evaluated their invasiveness. Compared with the other groups, the EcN@INX-2 + L group significantly inhibited the proliferation of tumor cells (Fig. 7e, row 3).

Photo-immunotherapy of tumors in vivo

Upon studying the immune response following the administration of each agent, we assessed the activation of DCs in tumor tissue. The results from flow cytometry indicated that the EcN@INX-2 + L group exhibited enhanced maturation of DCs (15.5% $MHC\text{-}II^+CD11c^+$ DCs), achieving a 4.62-fold, 1.72-fold and 1.69-fold increase compared to the control group (3.4%), the EcN group (8.9%) and the INX-2 + L group (9.2%) respectively (Figs. 8a, d and Supplementary Fig. 18a). Cytotoxic T lymphocytes (CTL) ($CD3^+$ $CD8^+$ T cells) and helper T cells ($CD3^+$ $CD4^+$ T cells) played a crucial role in adaptive immunity regulation. As demonstrated in Figs. 8c, f and Supplementary Fig. 18b, the proportion of activated $CD3^+CD8^+$ T cells in the EcN@INX-2 + L group (22.3%) was 3.66-fold, 1.91-fold and 2.14-fold higher than that in the control, EcN and INX-2 + L groups respectively. Furthermore, in addition to recruiting CTLs, the EcN@INX-2 + L group also prompted a significant proliferation of helper T cells (17.1%) within the tumors, resulting in a 3.33-fold increase in comparison to the control group (Fig. 8b, e). These findings suggest that the EcN@INX-2 + L group effectively triggered the immune response, which represents a critical step in initiating anti-tumor immunity. Furthermore, representative biomarkers of ICD, such as HMGBl and etco-CRT, were examined in tumor sections using immunofluorescence staining. A significant reduction in nuclear HMGBl expression and increased etco-CRT expression were observed in the EcN@INX-2 + L group (Fig. 8g). Additionally, immunofluorescence staining demonstrated that tumor sections from the EcN@INX-2 + L group exhibited abundant $CD11c^+$ DC cells, $CD4^+$ helper T cells and $CD8^+$ cytotoxic T cells (Fig. 8h). These results collectively suggest that EcN@INX-2 + L effectively stimulated anti-tumor immune responses, augmented the presence of positive immune responders, ultimately restrained tumor growth.

Proteomics analysis

To elucidate the molecular mechanism of the EcN@INX-2 + L group, we conducted quantitative proteomics analysis to investigate the differential expression levels of proteins in CT26 tumor tissues of Balb/c female mice following treatments (PBS and EcN@INX-2 + L). We collected three biological replicate samples of CT26 tumor tissue for each treatment condition and identified 7444 proteins using liquid chromatography-tandem mass spectrometry (LC-MS/MS). Among these, 1316 proteins exhibited differential expression ($FC \geq 2$ or $FC \leq 1/2$, $p < 0.05$) between the EcN@INX-2 + L group and the control group, with 754 up-regulated and 562 down-regulated proteins (Supplementary Fig. 19 and 20). Gene ontology (GO) analysis of these differentially expressed proteins in biological processes indicated significantly higher up-regulation of proteins associated with stimulus response, inflammatory response, immune system and antioxidant activity in the EcN@INX-2 + L group compared to the control group (Figs. 9a and Supplementary Fig. 21). Furthermore, significantly elevated levels of proteins linked to heat shock, oxidative stress, cell death, inflammatory response, bacteria infection and immune response were observed in the EcN@INX-2 + L group (Fig. 9b). Figure 9c displays the heat map of the top 30 highly expressed proteins in the EcN@INX-2 + L group after treatment compared to the control group. The Venn diagram demonstrated a clear overlap among proteins associated with bacterial infection, inflammatory response and immune response (Fig. 9d). Additionally, this pattern is supported by the protein-protein interaction (PPI) network (Fig. 9e). In conclusion, these proteomics data indicate that EcN@INX-2 + L stimulated multiple immune processes, thereby activating anti-tumor immunity.

Systemic toxicity evaluation of EcN@INX-2 in vivo

Female mice subjected to various treatments exhibited negligible differences in body weight (Supplementary Fig. 22), preliminarily suggesting that all treatments possessed good biosafety. Ultimately, the female mice were humanely euthanized, and blood and major organs were collected for further assessment of in vivo biosafety. Supplementary Fig. 23 exhibits the outcomes of blood biochemical analyses encompassing liver function indicators such as alanine aminotransferase (ALT), aspartate aminotransferase (AST) and albumin (ALB), alongside renal function markers including blood urea nitrogen (BUN), creatinine (CREA) and urea. The hepatic and renal function parameters of the mice were within the normal range, confirming that the bacterial drug delivery treatment intervention did not exert any significant adverse effects on liver or kidney function. In addition, most of the hematological parameters remained within the normal range (Supplementary Fig. 24), suggesting that the EcN@INX-2 + L group had good hematological compatibility. The analysis results indicated an absence of significant indications of injury or infection in female mice post various treatments, affirming their enduring biosafety. To delve deeper into systemic inflammation, C-reactive protein (CRP) levels were measured, revealing no indications of systemic infection induced by the EcN@INX-2 + L group (Supplementary Fig. 25). Evaluation of tissue damage in female mice was conducted through H&E staining, demonstrating no observable harm or inflammation in the vital organs

https://doi.org/10.1038/s41467-025-57533-y

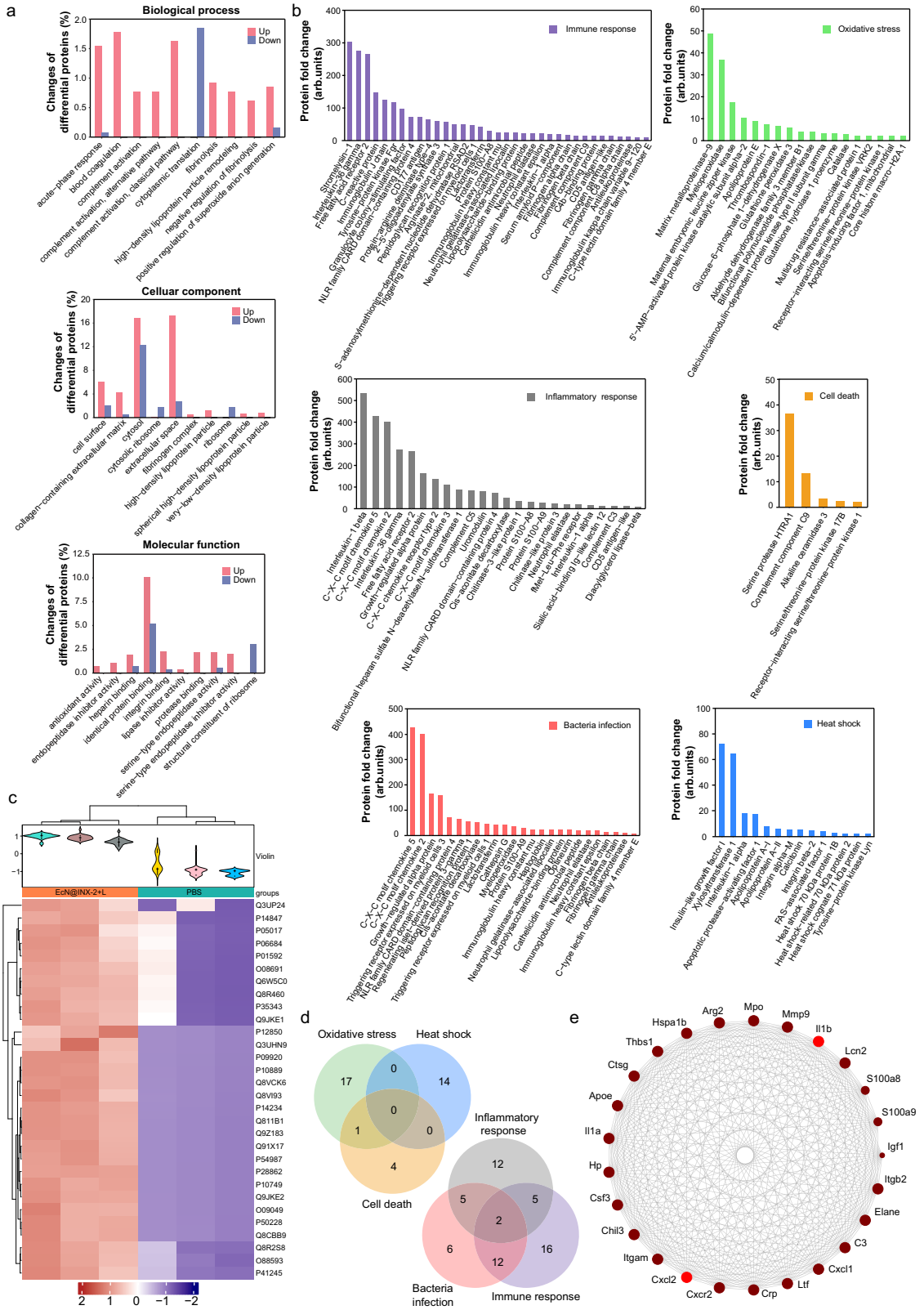

Fig. 9 | Proteomic quantitative analysis to explore the antitumor mechanism of EcN@INX-2. a Biological processes, cellular components, and molecular functions of diverse proteins were scrutinized through GO term enrichment analysis ($n = 3$ mice). **b** Bar charts representing the distinct proteins associated with the specific biological process of interest, as characterized by GO annotations ($n = 3$ mice). **c** Heat map showing top 30 highly expressed proteins. Statistical analyzes were performed using two-tailed Student's t-test. Box, median with whiskers at minimum and maximum values (fold change ≥ 2 or fold change ≤ 1/2, $P < 0.05$) ($n = 3$ mice). **d** Venn diagram delineated the distinct biological processes associated with heat shock and oxidative stress, as well as the intersecting biological processes related to bacterial infection, inflammatory response, and immune response ($n = 3$ mice). **e** The PPI of the top 25 differentially expressed proteins ($n = 3$ mice). Source data are provided as a Source Data file.

of tumor-bearing female mice across all treatment groups post-treatment, underscoring the substantial histocompatibility and high biosafety of the EcN@INX-2 + L group (Supplementary Fig. 26).

Discussion

Although tumor-targeted bacteria offer significant therapeutic potential, the molecular and histological heterogeneity of cancers suggests that a multifaceted therapeutic strategy may be required to address the limited effectiveness of any single treatment modality, including bacteria-based therapies. This study presents the synthesis of novel AIEgen (INX-2) through careful modulation of effective intramolecular charge transfer effect and the counter ion effect. INX-2 exhibited compelling properties including long-wavelength absorption, NIR-II fluorescence, excellent photothermal and PA properties, rendering it an ideal fluorescent molecule for multimodal phototheranostics in colon cancer. To facilitate efficient delivery and colon cancer targeting, INX-2 was further conjugated with the tumor-targeting bacteria EcN. In vivo assessments have abundantly illustrated that the final fabricated bionanomaterials can accomplish tumor hypoxic region targeting akin to an "AIEgen Bacteria Hybrid Bionic Robot" through NIR-II FLI-PAI-PTI multimodal imaging, and can also induce tumor ablation via phototherapeutic chelation. Given the convenience and feasibility of this bacterial modification strategy, our study proposes a biomimetic one-and-done photothermal nanoplatform that opens a promising avenue for enhancing anti-colon cancer efficacy. While our study used a subcutaneous tumor mouse model, which is a widely accepted model for the initial evaluation of NIR-II imaging agents, it does have limitations. The use of this model does not fully recapitulate the complexity of tumor microenvironments found in human cancers, particularly those that are deeply seated or in different anatomical locations. Furthermore, the penetration depth of NIR light in the subcutaneous model may not accurately reflect the situation in clinical settings where light scattering and absorption by tissue can significantly affect imaging depth and resolution. In conclusion, while our study provides valuable preliminary data on the use of NIR-II imaging, future research must address these limitations by employing more sophisticated animal models and leveraging the latest advancements in detector technology to fully realize the potential of NIR-II bioimaging in cancer research. Regarding future translation, several potential challenges, such as route of administration, intratumoral bacterial distribution mechanism, dose and frequency of bacteria modification, and safety issues, need to be systematically evaluated before considering clinical applications.

Methods

Ethical statements

All animal experimentation procedures are in accordance with the Regulations on the Administration of Laboratory Animals of the State Council of the People's Republic of China. Ethical approval for this study was obtained from the Experimental Animal Ethics Committee of the First Affiliated Hospital of Guangzhou Medical University (Approval number: 20230406). Mice were housed in a controlled environment maintained at approximately 22 °C, with a 12 h light/dark cycle. The relative humidity was maintained at an appropriate level (50%). Standard rodent chow and water were available ad libitum to ensure the well-being and normal physiological functions of the animals.

Materials

All solvents and reagents were purchased from commercial suppliers without further purification. 6-bromo-2,3-dihydro-1H-xanthene-4-carbaldehyde (purity 95%) was from Bide Pharmatech Ltd.(China). Bis(4-methoxyphenyl)amine (purity 98%), Cs_2CO_3 (purity 99%), $Pd_2(OAc)_2$ (purity 99%), tri-tert-butylphosphine tetrafluoroborate (purity 99%), Na_2SO_4 (purity 99%), DCFH-DA (purity 97%), MTT (purity 98%), Calcein, AM (purity 96%) and PI (purity 94%) were purchased from Sigma-Aldrich (Germany). LB broth and LB agar were from Sangon Biotech Co., Ltd. (China), and HMGB1 ELISA kits (CSB-E08225m) were obtained from Elabscience. Antifade mounting medium with DAPI was purchased from Beyotime Biotechnology (China). Antibodies used: ICD Immunofluorescence staining: Calreticulin Rabbit Monoclonal Antibody (1:200, Beyotime Biotechnology, Rabbit mAb, #AF1666); HMGB1 Rabbit Monoclonal Antibody (1:200, Beyotime Biotechnology, Rabbit mAb, #AG2167); Anti-CD11c Rabbit pAb (1:400, Servicebio Technology, #GB11059); Anti-CD4 Rabbit pAb (1:400, Servicebio Technology, #GB11064); Anti-CD8 alpha Rabbit pAb (1:500, Servicebio Technology, #GB114196); Alexa Fluor 488-labeled Goat Anti-Rabbit IgG(H + L) (1:500, Beyotime Biotechnology, Rabbit mAb, #A0423); Alexa Fluor 647-labeled Goat Anti-Rabbit IgG(H + L) (1:500, Beyotime Biotechnology, Rabbit mAb, #A0468). Flow cytometry: Fixable Viability Dye eFluor 780 (1:200, eBioscience, #65-0865-14); Brilliant Violet 510 anti-mouse CD45 Antibody (1:200, Biolegend, #103137); FITC anti-mouse CD3e Antibody (1:200, eBioscience, #16-0031-82); Super Bright 436 anti-mouse CD4 Antibody (1:200, eBioscience, #62-0042-82); PE anti-mouse CD8a Antibody (1:200, eBioscience, #12-0081-82); APC anti-mouse CD11c Antibody (1:200, eBioscience, #17-0114-82); PE anti-mouse MHC Class II (I-A/I-E) Antibody (1:200, eBioscience, #12-5321-81).

Characterization

NMR spectra were detected by Bruker 600 MHz NMR spectrometers. UV-Vis absorption spectra were acquired using a PerkinElmer Lambda 950 spectrophotometer. Photoluminescence spectra were obtained employing an Edinburgh FLS1000 fluorescence spectrophotometer. Transmission electron microscopy images were detected by a JEM-2100 Electron Microscope. Dynamic light scattering measurements were conducted using a Malvern Zetasizer Nano ZS90.

ROS generation of INX-2 in aqueous solution

Total ROS were detected by DCFH. DCFH-DA was hydrolyzed to DCFH activation solution (40 μM) by adding 1 mL of NaOH solution (10 mM) and 5 mL of PBS (pH 7.4) to 250 μL of DCFH-DA solution (1 mM, EtOH), which was then incubated at room temperature in darkness for 30 min. A solution comprising 125 μL DCFH activation solution (40 μM), 1 μL PS (1 mM) and 874 μL PBS was prepared. The fluorescence intensities of 100 μL of this solution were measured at various time points before and after laser irradiation (660 nm, 0.45 W cm^{-2}, 10 min) using a microplate reader (Ex = 488 nm, Em = 525 nm).

$O_2^{\cdot-}$ detection by DHR 123 and •OH detection by HPF. A blend consisting of 1 μL of either DHR 123 (5 mM) or HPF (5 mM), 1 μL of PS (1 mM), and 998 μL of PBS was prepared. The fluorescence intensities of 100 μL of this solution were measured at various time points before and after laser irradiation (660 nm, 0.45 W cm^{-2}, 10 min) using a microplate reader (Ex = 488 nm, Em = 525 nm).

$^1O_2$ detection by ABDA or SOSG. A mixture of 5 μL ABDA (10 mM), 1 μL PS (1 mM), and 994 μL PBS was prepared. The microplate reader documented the alteration in the UV absorption peak (350 nm - 420 nm) of 100 μL of the mixed solution after laser irradiation (660 nm, 0.45 W cm^{-2}, 10 min).

A mixed solution of 1 μL of SOSG (5 mM), 1 μL of PS (1 mM), and 998 μL of PBS was prepared. The fluorescence intensities of 100 μL of this solution were measured at various time points before and after laser irradiation (660 nm, 0.45 W cm^{-2}, 10 min) using a microplate reader (Ex = 488 nm, Em = 525 nm).

Photothermal effect

To study the photothermal behavior of INX-2 under laser irradiation, 200 μL of INX-2 solution was exposed to the laser irradiation (660 nm,

0.45 W cm^{-2}, 5 min) and captured using a FLIR E6 thermal imaging camera (FLIR thermal camera Systems, Inc., USA). The photothermal conversion efficiency (η) was calculated according to the Eq. (1)[63,64]:

$$\eta = \frac{hS \times (T_{max} - T_{surr}) - Q_{dis}}{I \times (1 - 10^{-A_{660nm}})} \quad (1)$$

where S is the surface area of the vessel, h is the heat-transfer coefficient, T_{max} is the maximum laser-triggered temperature, T_{surr} is the room temperature, Q_{dis} is the heat dissipation due to light absorption by the centrifuge tube, I is the intensity of laser (0.45 W cm^{-2}), and A_{660nm} is the absorbance of INX-2 at 660 nm. The value of hS can be calculated by Eq. (2)[64]:

$$hS = \frac{\sum_i m_i C_{p,i}}{\tau s} \quad (2)$$

where τs is the time constant of the sample system; compared with solvent (water). m_{water} is the solution mass and $C_{p,\ water}$ is specific heat capacity of the solution ($C_{p,\ water}$ = 4.2 J/g °C), respectively.

PA imaging of INX-2

The intensity changes of INX-2 in the 680-970 nm wavelength range were detected using a PA imaging system (VEVO LAZR-X, Fujifilm VisualSonics Inc., Canada).

Density functional theory calculations

The DFT and TD-DFT theoretical methods were used for the ground state and excited state computations by using the Gaussian 09 program (revision D.01)[65]. The geometry of compound INX-2 in the ground state was energetically optimized using B3LYP functional and 6-31 G(d, p) basis set. TD-DFT was utilized at the same level of theory to calculate excitation energies for electronically excited singlet and triplet states. SOC matrix elements between the singlet and triplet were calculated on ORCA 4.2.1 program[66–68] with B3LYP functional and 6-31 G(d, p) basis set. In all calculations above, the solvent effect of DMSO was considered by the Solvation Model Based on Density (SMD) solvation model.

Cell line and bacteria

CT26 cells were acquired from the National Collection of Authenticated Cell Cultures (NCACC, China). *Escherichia coli* Nissle 1917 was acquired from the Guangdong Microbial Culture Collection Center (GDMCC, China).

Preparation of EcN@INX-2

Bacteria (EcN) were harvested by centrifugation (3500 × *g*, 3 min). The supernatant was discarded, and the pelllet suspended in PBS containing various concentrations of INX-2. The suspension was subsequently incubated for 5–30 min. The supernatant was then discarded by centrifugation (3500 × *g*, 3 min) and resuspended in PBS.

CLSM imaging of EcN@INX-2

A suspension of EcN bacterial cells at a concentration of 5×10^8 CFU mL^{-1} was added to 1 mL of PBS with 5 μM INX-2. The bacterial suspension was incubated on a shaker at 37 °C and 200 rpm for 30 min. Subsequently, the suspension was centrifuged (3500 × *g*, 3 min) to remove the supernatant, and the pellet was resuspended in a small amount of PBS. Images were captured using a CLSM (ZEISS LSM 980 with Airyscan 2, Germany).

ROS generation and photothermal effect of EcN@INX-2 in aqueous solution

A solution comprising 125 μL DCFH activation solution (40 μM), 100 μL EcN@INX-2 (10 μM), and 775 μL PBS was prepared. The fluorescence intensities of 100 μL of this solution were measured at various time points before and after laser irradiation (660 nm, 0.45 W cm^{-2}, 10 min) using a microplate reader (Ex = 488 nm, Em = 525 nm). To study the photothermal behavior of EcN@INX-2 under laser irradiation, 200 μL of EcN@INX-2 (50 μM) solution was placed under the laser irradiation (660 nm, 0.45 W cm^{-2}, 5 min) and captured using a FLIR E6 Thermal Imaging Camera.

Antibacterial tests of INX-2

Using a bacterial loop, a single colony of EcN from LB agar was inoculated into LB broth and shaken overnight at 37 °C and 200 rpm on a temperature-controlled shaker. Bacterial fluids were washed twice by centrifugation (3500 × *g*, 3 min). The supernatant was discarded and the pellet was resuspended with PBS followed by centrifugation (3500 × *g*, 3 min). A bacterial suspension working solution (10^9 CFU mL^{-1}, OD_{600} = 1) was prepared using PBS. Different concentrations of INX-2 were added to the bacterial suspension (5×10^8 CFU mL^{-1}, 100 μL) and then co-incubated in a constant temperature shaker (200 rpm, 30 min). The bacterial suspensions were divided into laser irradiation (660 nm, 0.45 W cm^{-2}, 10 min) and dark groups. The treated bacterial suspension was diluted proportionally and spread in LB-agar plates, and incubated at 37 °C for 16-24 h before being photographed and counted. The treated bacterial suspensions were stained using the SYTO 9/PI, Live/Dead Bacteria Double Staining Kit and visualized by CLSM.

Cell viability assay

The MTT assay was employed to assess the cytotoxic effects of EcN@INX-2. Various concentrations of EcN@INX-2 suspensions were added into the upper compartment of a Transwell® (pore size 0.4 μm, Corning Costar), with the target cells seeded in the lower compartment. Subsequently, the upper chamber underwent irradiation with a laser irradiation (660 nm, 0.45 W cm^{-2}, 10 min). Following an additional 12 h incubation period, cellular viability was evaluated using the MTT assay.

Characterization of immunologic cell death

CT26 cells (1.5×10^5 cells well^{-1}) were cultured in 24-well plates with coverslips for 12 h, after which either PBS or EcN@INX-2 (EcN: 1×10^8 CFU mL^{-1}, 100 μL; INX-2: 1 μM) was added. The culture was incubated for 6 h. The cells were then rinsed with PBS and either kept in the dark or exposed to a laser irradiation (660 nm, 0.45 W cm^{-2}, 10 min). After a further 12 h of incubation, the cells were fixed in a 4% paraformaldehyde solution on ice bath temperature for 20 min. Subsequently, the cells were incubated with an anti-calreticulin antibody or an anti-HMGB1 antibody at 4 °C overnight. Subsequently, the cells were incubated with Alexa Fluor 488-labeled Goat Anti-Rabbit IgG (H + L) for an additional 2 h at room temperature. The nuclei were subsequently stained with DAPI in an antifade mounting medium. Following this, the cells were imaged using CLSM to assess the exposure of ecto-CRT and the release of HMGB1 from the nuclei.

To detect extracellular HMGB1, CT26 cells (3×10^5 cells well^{-1}) were inoculated into 6-well plates and cultured in medium containing EcN@INX-2 for 6 h at 37 °C. Following this, the cells were irradiated with a laser (660 nm, 0.45 W cm^{-2}, 10 min) and continued to be cultured for an additional 12 h. The culture supernatant was collected by centrifugation at 1000 × *g* for 10 min at 4°C. The concentration of HMGB1 released into the supernatant was quantified using the HMGB1 ELISA kit according to the manufacturer's instructions.

The evaluation of EcN@INX-2 in 3D tumor spheroids

Agarose was dissolved in cell culture medium to prepare a 2% solution. The bottom of a 96-well plate was coated with 60 μL of the agarose solution. CT26 cells (2×10^3 cells well^{-1}) were seeded into the agarose-coated plates and cultured for 5 days. Once a 3D tumor sphere of

approximately 180-200 μm had formed, it was transferred to an agarose-coated confocal dish and subjected to treatment with INX-2 or EcN@INX-2 for 12 h. The cell spheres in the confocal dish were imaged using the Z-stack function of a confocal laser scanning microscope (Zeiss-LSM-980, Germany). For phototherapy testing on 3D tumor spheroids, the spheroids were incubated with different formulations for 24 h, followed by laser irradiation (660 nm, 0.45 W cm^{-2}, 10 min). The spheroids were stained using a Live/Dead cell viability assay kit and imaged using CLSM.

Animals and subcutaneous tumor model

BALB/c female mice (4 weeks old) were obtained from Zhuhai Bestest Biotechnology Co., Ltd. (China). 100 μL of CT26 cells (1×10^7 cells mL^{-1}) were injected subcutaneously into the the right thigh root of the mice. Tumor volume in the mice was calculated using the Eq. (3)[7,8]:

$$\text{Volume}(mm^3) = \text{Length}(mm) \times \text{Width}(mm) \times \text{Width}(mm)/2 \quad (3)$$

In compliance with the regulations and guidelines set forth by the Experimental Animal Ethics Committee, the mice in this study were to be euthanized using carbon dioxide anesthesia when the tumor volume reached 2000 mm^3 or if the tumor burden affected animal welfare. Notably, the tumors in the mice throughout this study did not surpass the predetermined maximum volume.

In vivo biodistribution and tumor retention of EcN

The in vivo biodistribution of EcN (1×10^8 CFU mL^{-1}, 100 μL) was evaluated by administering it intravenously to female mice once their tumors had grown to approximately 100 mm^3. Female mice were euthanized at different time intervals, and tumors as well as major organ tissues (heart, liver, spleen, lungs, and kidneys) were harvested for cryomilling. The resulting tissue homogenate was serially diluted and plated onto LB agar, followed by photography and colony counting.

In vivo multi-modal imaging

CT26 tumor-bearing female mice were administered with EcN@INX-2 (EcN: 5×10^8 CFU mL^{-1}, INX-2: 150 μg mL^{-1}) in PBS via intravenous injection. The female mice were anesthetized with 2% isoflurane in oxygen. NIR-I fluorescence images were acquired with 710 nm excitation and 840 nm emission filters after anesthesia induction by IVIS Lumina XRMS Series III in vivo tracking system (PerkinElmer, USA). NIR-II fluorescence images were collected using a full spectrum animal in vivo imaging system (710 nm excitation laser with a long pass filter of 1075 nm), AniView Phoenix 600 (Guangzhou Biolight Biotechnology Co., Ltd., China). The fluorescence intensity was analyzed using the software provided by the manufaturer. Similarly, in vivo PA imaging was also performed 1 day post-injection by the PA imaging system, Vevo LAZR (Fujifilm VisualSonics Inc., Canada). To confirm the in vivo photothermal property, thermographic images of the tumor were performed on the mice (at 1 day post-injection) exposed to the laser irradiation (660 nm, 0.45 W cm^{-2}, 10 min), which were captured using a FLIR E6 Thermal Imaging Camera (FLIR thermal camera Systems, Inc., USA) during laser irradiation.

In vivo anti-tumor experiments

When the tumor volumes were about 150 mm^3, CT26 tumor-bearing female mice were randomly divided into seven groups: (I) PBS group; (II) PBS plus laser (660 nm, 0.45 W cm^{-2}, 10 min) (PBS + L) group; (III) EcN group; (IV) INX-2 group; (V) INX-2 plus laser (INX-2 + L) group; (VI) EcN@INX-2 group; (VII) EcN@INX-2 plus laser (EcN@INX-2 + L) group. Female mice were administeredEcN@INX-2 (200 μL, EcN: 5×10^8 CFU mL^{-1}, INX-2: 150 μg mL^{-1}) via intravenous injection. Mouse growth was monitored by the measurement of tumor volume and body weight. Upon completion of the treatment period, mice were humanely euthanized, and tumor tissue was subsequently harvested for photography and weight determination. The collected mouse tumor tissues were fixed and embedded in paraffin for histological analysis to evaluate the anti-tumor efficacy.

In vivo immune cell analysis by flow cytometry

Tumors from female CT26 tumor-bearing mice, which had been subjected to various treatments, were harvested on day 13 and processed into single-cell suspensions via mechanical milling. The resulting cell suspension was then centrifuged at 1000 × *g* for 3 min, and the pellet was collected and treated with erythrocyte lysis buffer for 2-3 min. Following this, the suspension was centrifuged at 2000 × *g* for 2 min at room temperature to eliminate erythrocytes, rinsed twice with PBS, treated with an Fc Antibody Blocker, and centrifuged (2000 × *g*, 2 min) twice with PBS in preparation for further antibody staining. A portion of the cells was incubated with a mixture comprising FVD eFluor-780, anti-MHC-II-PE, anti-CD11c-APC, and anti-CD45-BV510 antibodies for 30 min at 4 °C, then washed three times with PBS and up-sampled for the analysis of mature DCs via flow cytometry. The remaining cells were incubated with an antibody mixture containing FVD efluor-780, anti-CD3-FITC, anti-CD4-Super Bright 600, and anti-CD8-APC for 30 min at 4 °C, followed by three washes with PBS, and analyzed for $CD3^+CD8^+$ T cells and $CD3^+CD4^+$ T cells by flow cytometry.

In vivo systemic toxicity evaluation

Serum and anticoagulated blood were collected on day 13 for blood biochemistry and routine blood examination, respectively. At the end of treatment period, paraffin sections of major organs (heart, liver, spleen, lungs and kidneys) from mice were prepared for H&E staining and analysis.

Proteomics analysis

Tumor tissues from the PBS and EcN@INX-2 + L groups ($n = 3$) were collected on day 13 and subjected to quantitative proteomics analysis at Shanghai OE Biotech Co., Ltd. (China). Proteins were considered to be differentially expressed if the fold-change between the experimental and control groups was greater than 2 or less than 0.5 ($p < 0.05$).

Statistical analysis

The data results are expressed as the mean ± standard deviation (SD). Statistical analyses were conducted using GraphPad Prism 9.3.1, with one-way ANOVA for multiple comparisons and two-tailed Student's *t*-test for comparisons between two groups. A significance level of $p < 0.05$ was utilized for determining statistical significance.

Reporting summary

Further information on research design is available in the Nature Portfolio Reporting Summary linked to this article.

Data availability

The proteomics raw data in this study have been deposited in the iProX database under accession code IPX0009941000 (www.iprox.cn). Source Data are provided with this paper. The remaining data are available within the article, supplementary information, or source data files. All data underlying this study are available from the corresponding author upon request. Source data are provided with this paper.

References

1. Bray, F. et al. Global cancer statistics 2022: GLOBOCAN estimates of incidence and mortality worldwide for 36 cancers in 185 countries. *Ca-Cancer J. Clin.* **74**, 229–263 (2024).
2. Zhan, T. et al. Digestive cancers: mechanisms, therapeutics and management. *Signal transduct. target. ther.* **10**, 24 (2025).

3. Zhang, H., Liu, Y. & Qu, S. Recent advances in photo-responsive carbon dots for tumor therapy. *Responsive Mater* **2**, e20240012 (2024).
4. Tang, Y., Wang, Z. & Li, Q. Pyroptosis of breast cancer stem cells and immune activation enabled by a multifunctional prodrug photosensitizer. *Adv. Funct. Mater.* **34**, 2405367 (2024).
5. Overchuk, M., Weersink, R. A., Wilson, B. C. & Zheng, G. Photodynamic and photothermal therapies: synergy opportunities for nanomedicine. *ACS Nano* **17**, 7979–8003 (2023).
6. Li, H., Kim, Y., Jung, H., Hyun, J. Y. & Shin, I. Near-infrared (NIR) fluorescence-emitting small organic molecules for cancer imaging and therapy. *Chem. Soc. Rev.* **51**, 8957–9008 (2022).
7. Yang, X. et al. Donor–acceptor modulating of ionic AIE photosensitizers for enhanced ROS generation and NIR-II emission. *Adv. Mater.* **36**, 2402182 (2024).
8. Kang, X. et al. A photo-triggered self-accelerated nanoplatform for multifunctional image-guided combination cancer immunotherapy. *Nat. Commun.* **14**, 5216 (2023).
9. Guo, S. et al. Combined photothermal and photodynamic therapy for cancer treatment using a multifunctional graphene oxide. *Pharmaceutics* **14**, 1365 (2022).
10. He, M. et al. Phototherapeutic nanoagents for cancer immunotherapy. *Prog. Mater. Sci.* **147**, 101347 (2025).
11. Meier, P., Legrand, A. J., Adam, D. & Silke, J. Immunogenic cell death in cancer: targeting necroptosis to induce antitumour immunity. *Nat. Rev. Cancer* **24**, 299–315 (2024).
12. Sen, S. et al. Metal-based anticancer agents as immunogenic cell death inducers: the past, present, and future. *Chem. Soc. Rev.* **51**, 1212–1233 (2022).
13. Galluzzi, L., Guilbaud, E., Schmidt, D., Kroemer, G. & Marincola, F. M. Targeting immunogenic cell stress and death for cancer therapy. *Nat. Rev. Drug Discovery* **23**, 445–460 (2024).
14. Kim, S., Tachikawa, T., Fujitsuka, M. & Majima, T. Far-red fluorescence probe for monitoring singlet oxygen during photodynamic therapy. *J. Am. Chem. Soc.* **136**, 11707–11715 (2014).
15. Catanzaro, E., Beltrán-Visiedo, M., Galluzzi, L. & Krysko, D. V. Immunogenicity of cell death and cancer immunotherapy with immune checkpoint inhibitors. *Cell. Mol. Immunol.* **22**, 24–39 (2025).
16. Pan, Y. et al. Immunological nanomaterials to combat cancer metastasis. *Chem. Soc. Rev.* **53**, 6399–6444 (2024).
17. Zhang, S. et al. Emerging photodynamic nanotherapeutics for inducing immunogenic cell death and potentiating cancer immunotherapy. *Biomaterials* **282**, 121433 (2022).
18. Chen, Q., Chen, M. & Liu, Z. Local biomaterials-assisted cancer immunotherapy to trigger systemic antitumor responses. *Chem. Soc. Rev.* **48**, 5506–5526 (2019).
19. Krysko, D. V. et al. Immunogenic cell death and DAMPs in cancer therapy. *Nat. Rev. Cancer* **12**, 860–875 (2012).
20. Li, X., Lovell, J. F., Yoon, J. & Chen, X. Clinical development and potential of photothermal and photodynamic therapies for cancer. *Nat. Rev. Clin. Oncol.* **17**, 657–674 (2020).
21. Chen, C. et al. Massively Evoking Immunogenic cell death by focused mitochondrial oxidative stress using an AIE luminogen with a twisted molecular structure. *Adv. Mater.* **31**, 1904914 (2019).
22. Zhang, C. et al. Semiconducting polymer nano-PROTACs for activatable photo-immunometabolic cancer therapy. *Nat. Commun.* **12**, 2934 (2021).
23. Yang, M. et al. State-of-the-art self-luminescence: a win–win situation. *Chem. Soc. Rev.* **51**, 8815–8831 (2022).
24. Li, H. et al. Recent advances of aggregation-induced emission in body surface organs. *Aggregate* **5**, e470 (2024).
25. Li, J. et al. Supramolecular materials based on AIE luminogens (AIEgens): construction and applications. *Chem. Soc. Rev.* **49**, 1144–1172 (2020).
26. Yang, S.-Y., Chen, Y., Kwok, R. T. K., Lam, J. W. Y. & Tang, B. Z. Platinum complexes with aggregation-induced emission. *Chem. Soc. Rev.* **53**, 5366–5393 (2024).
27. Crosby, D. et al. Early detection of cancer. *Science* **375**, eaay9040 (2022).
28. Rong, J. & Liu, Y. Advances in medical imaging techniques. *BMC Methods* **1**, 10 (2024).
29. Yin, J. et al. Nanosecond-resolution photothermal dynamic imaging via MHZ digitization and match filtering. *Nat. Commun.* **12**, 7097 (2021).
30. Wang, F., Zhong, Y., Bruns, O., Liang, Y. & Dai, H. In vivo NIR-II fluorescence imaging for biology and medicine. *Nat. Photonics* **18**, 535–547 (2024).
31. Lin, L. & Wang, L. V. The emerging role of photoacoustic imaging in clinical oncology. *Nat. Rev. Clin. Oncol.* **19**, 365–384 (2022).
32. Bai, J.-W., Qiu, S.-Q. & Zhang, G.-J. Molecular and functional imaging in cancer-targeted therapy: current applications and future directions. *Signal transduct. target. ther.* **8**, 89 (2023).
33. Wang, C. et al. Advanced nanotechnology leading the way to multimodal imaging-guided precision surgical therapy. *Adv. Mater.* **31**, 1904329 (2019).
34. Tang, Y. et al. Pyroptosis-mediated synergistic photodynamic and photothermal immunotherapy enabled by a tumor-membrane-targeted photosensitive dimer. *Adv. Mater.* **35**, 2300232 (2023).
35. Tang, Y., Wang, X., Chen, S. & Li, Q. Photoactivated theranostic nanomaterials based on aggregation-induced emission luminogens for cancer photoimmunotherapy. *Responsive Mater* **2**, e20240003 (2024).
36. Pan, Y. et al. Near-infrared laser-activated aggregation-induced emission nanoparticles boost tumor carbonyl stress and immunotherapy of breast cancer. *Aggregate* **5**, e432 (2024).
37. Kwon, S.-Y., Thi-Thu Ngo, H., Son, J., Hong, Y. & Min, J.-J. Exploiting bacteria for cancer immunotherapy. *Nat. Rev. Clin. Oncol.* **21**, 569–589 (2024).
38. El Tekle, G. & Garrett, W. S. Bacteria in cancer initiation, promotion and progression. *Nat. Rev. Cancer* **23**, 600–618 (2023).
39. Gurbatri, C. R., Arpaia, N. & Danino, T. Engineering bacteria as interactive cancer therapies. *Science* **378**, 858–864 (2022).
40. Akolpoglu, M. B. et al. Magnetically steerable bacterial microrobots moving in 3D biological matrices for stimuli-responsive cargo delivery. *Sci. Adv.* **8**, eabo6163 (2022).
41. Zhang, Y. et al. Stimulation of tumoricidal immunity via bacteriotherapy inhibits glioblastoma relapse. *Nat. Commun.* **15**, 4241 (2024).
42. Schmidt, C. K., Medina-Sánchez, M., Edmondson, R. J. & Schmidt, O. G. Engineering microrobots for targeted cancer therapies from a medical perspective. *Nat. Commun.* **11**, 5618 (2020).
43. Wu, Q. et al. Inhibition of tumor metastasis by liquid-nitrogen-shocked tumor cells with oncolytic viruses infection. *Adv. Mater.* **35**, 2212210 (2023).
44. Deng, G. et al. Natural-killer-cell-inspired nanorobots with aggregation-induced emission characteristics for near-infrared-II fluorescence-guided glioma theranostics. *ACS Nano* **14**, 11452–11462 (2020).
45. Bressler, E. M. & Wong, W. W. Engineered bacteria guide T cells to tumors. *Science* **382**, 154–155 (2023).
46. Guo, H. et al. Integrating bacteria with a ternary combination of photosensitizers for monochromatic irradiation-mediated photoacoustic imaging-guided synergistic photothermal therapy. *ACS Nano* **17**, 5059–5071 (2023).
47. Xue, K., Wang, L. & Liu, J. Surface modification of bacteria to optimize immunomodulation for advanced immunotherapy. *ChemMedChem* **18**, e202200574 (2023).
48. Chen, W. et al. Bacteria-driven hypoxia targeting for combined biotherapy and photothermal therapy. *ACS Nano* **12**, 5995–6005 (2018).

49. Harimoto, T. et al. A programmable encapsulation system improves delivery of therapeutic bacteria in mice. *Nat. Biotechnol.* **40**, 1259–1269 (2022).
50. Rembacken, B. J., Snelling, A. M., Hawkey, P. M., Chalmers, D. M. & Axon, A. T. R. Non-pathogenic Escherichia coli versus mesalazine for the treatment of ulcerative colitis: a randomised trial. *Lancet* **354**, 635–639 (1999).
51. Chen, H. et al. Advances in Escherichia coli Nissle 1917 as a customizable drug delivery system for disease treatment and diagnosis strategies. *Mater. Today Bio* **18**, 100543 (2023).
52. Toso, J. F., et al. Phase I study of the intravenous administration of attenuated Salmonella typhimurium to patients with metastatic melanoma. *J. Clin. Oncol.* **20**, 142–152 (2002).
53. Yan, D. et al. Multimodal imaging-guided photothermal immunotherapy based on a versatile NIR-II aggregation-induced emission luminogen. *Angew. Chem., Int. Ed.* **61**, e202202614 (2022).
54. Grimme, S., Antony, J., Ehrlich, S. & Krieg, H. A consistent and accurate ab initio parametrization of density functional dispersion correction (DFT-D) for the 94 elements H-Pu. *J. Chem. Phys.* **132**, 154104 (2010).
55. Zhang, L. et al. Integration of AIEgens into covalent organic frameworks for pyroptosis and ferroptosis primed cancer immunotherapy. *Nat. Commun.* **14**, 5355 (2023).
56. Ji, A. et al. Acceptor engineering for NIR-II dyes with high photochemical and biomedical performance. *Nat. Commun.* **13**, 3815 (2022).
57. Yu, L. et al. Photocatalytic superoxide radical generator that induces pyroptosis in cancer cells. *J. Am. Chem. Soc.* **144**, 11326–11337 (2022).
58. Cen, P. et al. Aggregation-induced emission luminogens for in vivo molecular imaging and theranostics in cancer. *Aggregate* **4**, e352 (2023).
59. Ding, X. et al. Defect engineered bioactive transition metals dichalcogenides quantum dots. *Nat. Commun.* **10**, 41 (2019).
60. Hu, F., Xu, S. & Liu, B. Photosensitizers with aggregation-induced emission: Materials and Biomedical Applications. *Adv. Mater.* **30**, 1801350 (2018).
61. Wang, D. et al. Microbial synthesis of Prussian blue for potentiating checkpoint blockade immunotherapy. *Nat. Commun.* **14**, 2943 (2023).
62. Wu, W. et al. Bacterial metabolism-initiated nanocatalytic tumor immunotherapy. *Nano-Micro Lett* **14**, 220 (2022).
63. Lü, B. et al. Stable radical anions generated from a porous perylenediimide metal-organic framework for boosting near-infrared photothermal conversion. *Nat. Commun.* **10**, 767 (2019).
64. Gao, S. et al. Albumin tailoring fluorescence and photothermal conversion effect of near-infrared-II fluorophore with aggregation-induced emission characteristics. *Nat. Commun.* **10**, 2206 (2019).
65. Frisch, M., et al. *Gaussian 09, revision D.01; Gaussian, Inc.*, Wallingford, CT, (2013).
66. Neese, F. The ORCA program system. *WIREs Comput. Mol. Sci.* **2**, 73–78 (2012).
67. Neese, F. Software update: the ORCA program system, version 4.0. *WIREs Comput. Mol. Sci.* **8**, e1327 (2018).
68. Neese, F., Wennmohs, F., Becker, U. & Riplinger, C. The ORCA quantum chemistry program package. *J. Chem. Phys.* **152**, 224108 (2020).

Acknowledgements

This work was under financial support from the National Natural Science Foundation of China (22275040 (Y.L.)). Shenzhen Key Laboratory of Functional Aggregate Materials (ZDSYS20211021111400001 (B.Z.T.)), the Science Technology Innovation Commission of Shenzhen Municipality (KQTD20210811090142053 (B.Z.T.), JCYJ20220818103007014 (B.Z.T.)). We acknowledge Shanghai OE Biotech Co., Ltd. (Shanghai, China) for their support in conducting quantitative proteomic analysis.

Author contributions

L.Z., Y.L., G.L., and B.Z.T. conceived and designed the study. L.Z., Y.W., W.Z., Y.C., and J.S. performed the in vitro experiments and in vivo experiments. G.S. assisted in the chemical synthesis. D.W. performed the theoretical calculation. L.Z., Y.L., and B.Z.T. analyzed the data and participated in the discussion. Y.L. and B.Z.T. conceived and obtained funding for the project. Y.L. and L.Z. oversaw the research. L.Z. and Y.L. wrote the paper. All authors discussed the results and have approved the final version of the paper.

Competing interests

The authors declare no competing interests.

Additional information

Supplementary information The online version contains supplementary material available at https://doi.org/10.1038/s41467-025-57533-y.

Correspondence and requests for materials should be addressed to Guoxin Li, Ben Zhong Tang or Ying Li.

Peer review information *Nature Communications* thanks the anonymous reviewer(s) for their contribution to the peer review of this work. A peer review file is available.